## Performance evaluation of proprietary drainage components and sheathing membranes when subjected to climate loads, task 3: hygrothermal model benchmarking

Saber, Hamed H.; Maref, Wahid


*Client Report (National Research Council of Canada. Construction), 2015-03-15*

NRC·CNRC CONSTRUCTION

# Performance Evaluation of Proprietary Drainage Components and Sheathing Membranes when Subjected to Climate Loads

## Task 3 — Hygrothermal Model Benchmarking

Hamed H. Saber and Wahid Maref

15 March, 2015

National Research Council Canada
Conseil national de recherches Canada

Canada

# Table of Contents

# List of Figures

# List of Tables

# Summary

A benchmark assembly and a series of ten client wall assemblies were developed as part of the project "Performance Evaluation of Proprietary Drainage Components and Sheathing Membranes when Subjected to Climate Loads".

The purpose of this project was to assess the performance of wall drainage components and sheathing membranes (drainage system) in their ability to provide sufficient drainage and drying in Canadian climates with a moisture index (MI) greater than 0.9 and less than 3400 degree-days, or MI greater than 1.0 and degree days ≥ 3400 (primarily coastal areas). In these regions, the 2010 National Building Code requires a capillary break behind all Part 9 claddings. Currently, acceptable solutions to the NBC capillary break requirement include:

(a) A drained and vented air space not less than 10 mm deep behind the cladding;

(b) An open drainage material, not less than 10 mm thick and with a cross-sectional area that is not less than 80% open, behind the cladding;

(c) A cladding loosely fastened, with an open cross section (i.e. vinyl, aluminum siding)

(d) A masonry cavity wall or masonry veneer constructed according to Section 9.20 (i.e. 25 mm vented air space)

In this project, the performance of proposed alternative solutions for the capillary break was compared through laboratory evaluation and modeling activities to the performance of a wall built to minimum code requirements. The proposed drainage system would be deemed an alternative solution to the capillary break requirement in the National Building Code for use with all code compliant Part 9 claddings provided it exhibits adequate moisture performance as compared to a NBC-compliant benchmark wall assembly.

**In This Report —** Benchmarking exercises are described to validate the NRC-Construction's hygrothermal model "hygIRC-C" that was used to undertake the computer modeling in this project. The model was also used in this project to design the experimental setup for the benchmarking exercises that permitted obtaining useful data needed for validating the model. Additionally, a brief description of the hygIRC-C model and a record of benchmarking exercises completed for this model are provided. The results show that the model predictions for the airflow in drainage spaces and the drying rate of cladding made of stucco are in good agreement with the experiential data.

In addition, the model was used to design a test apparatus that can be used to determine the air permeability of non-homogenous and highly permeable drainage media. A procedure for using this test apparatus together with the model and that allows determining the permeability coefficient of porous media is also provided.

# Acknowledgements

The report authors wish to extend their thanks to the Air Barrier Association of American (ABAA) for having managed and arranged support for this project and in particular, to Mr. Laverne Dalgleish for his highly proficient handling of all technical and non-technical issues that arose over the course of the project. As well, acknowledgment is made of project support, technical meeting participation and the many and very useful contributions made by the respective project partners, and that included:

Benjamin Obdyke Incorporated

Canadian Concrete Masonry Producers Association

Cosella-Dorken

DuPont Tyvek Weatherization Systems

HAL Industries Incorporated

Home Protection Office of British Columbia – HPO

Keene Building Products™

GreenGuard® Building Products (formerly Pactiv Building Products)

Roxul Incorporated

STO Corporation

TYPAR® Weather Protection System (Polymer Group Incorporated)

Our thanks are also extended to our colleagues within NRC-Construction for their technical support, advice, and feedback during the course of this project and who helped support the work described in this Task report including: M. Armstrong, S. Bundalo-Perc, S. M. Cornick, B. Di Lenardo, G. Ganapathy, T. Moore, P. Mukhopadhyaya, M. Nicholls, M.C. Swinton and D. Van Reenen.

# *Performance Evaluation of Proprietary Drainage Components and Sheathing Membranes when Subjected to Climate Loads –*

# Task 3 – Hygrothermal Model Benchmarking

Authored by:

Hamed H. Saber and Wahid Maref

## A Report for the

## AIR BARRIER ASSOCIATION OF AMERICA (ABAA)

**1600 BOSTON-PROVIDENCE Highway**
**WAYPOLE, MA 02081**
**USA**

**ATT: Mr. Laverne Dalgleish**

National Research Council Canada
Ottawa ON K1A 0R6 Canada

## 15 March, 2015

# *Performance Evaluation of Proprietary Drainage Components and Sheathing Membranes when Subjected to Climate Loads –*

## Task 3 – Hygrothermal Model Benchmarking

### Final Report Task 3

Hamed H. Saber and Wahid Maref

## 1.0 Background and Introduction

The objective of this project was to assess the hygrothermal performance of wall assemblies incorporating drainage components in respect to their ability to provide sufficient drainage and drying in Canadian climates having a moisture index greater than 1.0. In these climates, the 2010 National Building Code (NBC) requires a capillary break behind all Part 9 claddings. Currently, acceptable solutions to the NBC requirement for a capillary break include:

a) A drained and vented air space not less than 10 mm deep behind the cladding;
b) An open drainage material, not less than 10 mm thick and with a cross-sectional area that is not less than 80% open, behind the cladding;
c) A cladding loosely fastened, with an open cross section (i.e. vinyl, aluminum siding);
d) A masonry cavity wall or masonry veneer constructed according to Section 9.20 (i.e. 25 mm vented air space).

In this project, the hygrothermal performance of proposed alternative solutions for the capillary break was compared through laboratory evaluation and modeling activities to the performance of a wall (reference wall) built to minimum code requirements using the following performance criteria:

(a) RHT criterion, and;
(b) Mould index criterion.

If a proposed wall system incorporating drainage components exhibits adequate performance as compared to the reference wall, it will be deemed an alternative solution to the 2010 National Building Code requirement for a capillary break and can be used with all code compliant Part 9 claddings.

## 1.1 Project Overview

The project was realised through several tasks for which an overview is provided in Figure 1[*]. Given that the basis for assessing performance of the wall assemblies incorporating drainage components was results derived from hygrothermal simulation, the majority of the tasks relate to preparing information suitable for input to the hygrothermal simulation model, hygIRC-C.

[*] A list of all project reports for different tasks is provided in Appendix 1

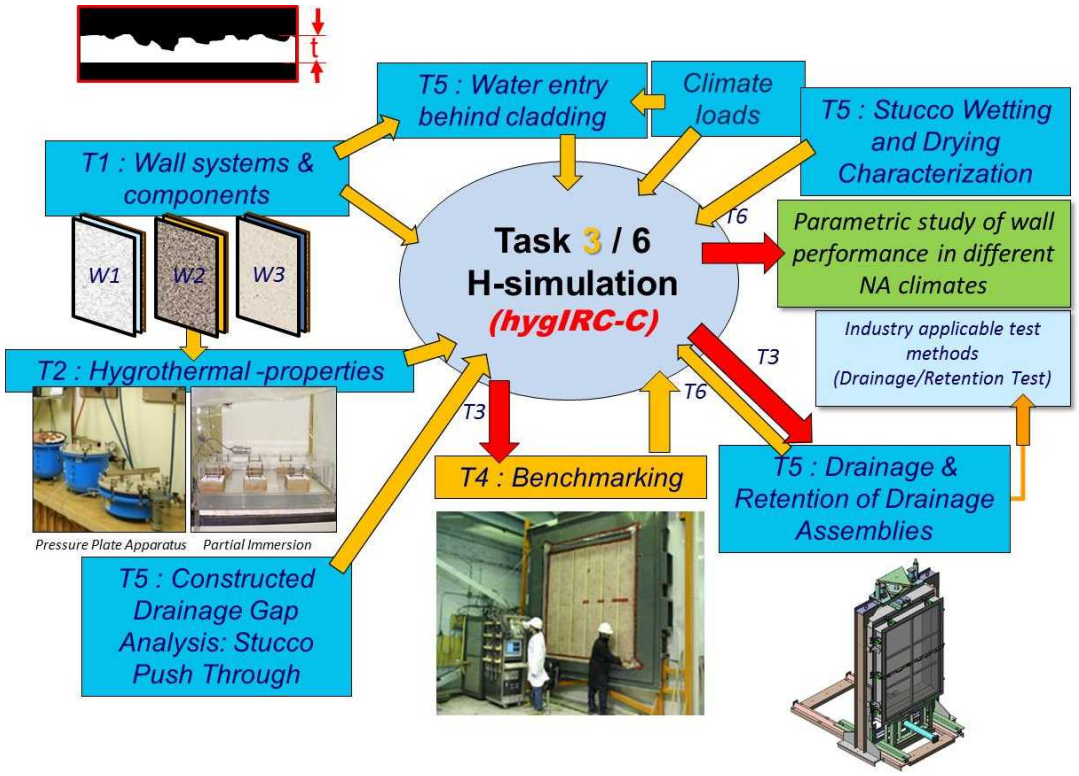


**Figure 1 – Project Overview**

As can be seen in Figure 1, Task 1 relates to defining the various wall assemblies and specification details necessary to develop a configuration of the wall, suitable for input to the model; results from this work are provided in the Task 1 report (Appendix 1). In Task 2, hygrothermal properties of key components of the wall assembly were evaluated and are reported in the Task 2 report; these properties were likewise input to the model. The third and fourth Tasks are linked together; in Task 4, experimental work was carried out on the cavity component of a generic wall assembly to permit benchmarking the variations in air flow in the cavity, as induced mechanically with an air pump, to that simulated with the model. A detailed description of the test apparatus, instrumentation, and methods used to benchmark the response of the model is provided in the Task 4 report together with the results from air flow measurements of several different cavity sizes as well as measurements on cavities in which were placed different drainage components.

Task 3 of the project, as described in this report, concerns the benchmarking exercise, in which the physics of phenomena being modelled and modeling assumptions are verified prior to undertaking hygrothermal simulations of wall assemblies by comparing results of selected experimental tests to that obtained from the model; the modelling assumptions would not be deemed adequate should significant deviations from the experimental results be evident. A description of the model and previous work undertaken to benchmark the model, are items provided in subsequent sections of this report. Task 5 relates to work undertaken to define climate loads and to provide an estimate of water entry through specified cladding and moisture retention within the cavity behind the cladding, in relation to a range of anticipated wind-driven rain loads. In the definitive task, Task 6, a parametric study was undertaken to assess the performance of the various wall assemblies that incorporated, or not, drainage components. Results provided in the Task 6 report form the basis for determining whether wall assemblies incorporating drainage components exhibit adequate performance as compared to the NBCC reference wall.

## 1.2 Description of Numerical Simulation Model – hygIRC-C

The NRC's hygrothermal model, hygIRC-C was used in this project to predict the hygrothermal performance on the basis of the risk of mould growth within wall assemblies having different drainage components when these walls were subjected to different climatic conditions as might occur across Canada. This model has been validated and used in a number of projects to assess the thermal and hygrothermal performance of different components of the building envelope (e.g. roofing, wall and fenestration systems). It is important to emphasize that the predictions by such a model for the airflow, temperature, and moisture (or relative humidity) distributions within a wall assembly, when subjected to a pressure differential (and resulting air leakage rate) across the assembly, are necessary to accurately determine the mould index in different layers of the wall assembly.

The hygIRC-C model simultaneously solves the highly nonlinear two-dimensional and three-dimensional Heat, Air and Moisture (HAM) equations that define values of heat, air and moisture transfer across building components. The HAM equations were discretized using the Finite Element Method (FEM). The hygIRC-C model has been extensively benchmarked in a number of other projects and has been used in several related studies to assess the thermal and hygrothermal performance of wall and roofing systems [1-31].

## 1.3 Record of Benchmarking hygIRC-C Model

In a previous project called "Wall Energy Rating (WER)", the three-dimensional version of this model was used to conduct numerical simulations for different full-scale 2 x 6 wall assemblies incorporating, or not, penetrations representative of a window installation, such that the effective thermal resistance (R-value) of the assemblies could be predicted, taking into consideration air leakage across the assembly. The stud cavity of these walls incorporated open cell polyurethane foam, closed cell spray polyurethane foam or glass fibre insulation. The predicted R-values for these walls were in good agreement (within ± 5% which are the same as the uncertainty of test data, see [3-6]) with the measured R-values that were obtained from testing in the NRC's Guarded Hot Box (GHB) according to the ASTM C-1363 standard test method [32].

The present model was also benchmarked against GHB test results according to the ASTM C-1363 standard test method [32] and heat flow meter according to the ASTM C-518 standard test method [33], and then used to conduct numerical simulations to investigate the effect of foil emissivity on the effective thermal resistance of different wall systems with foil bonded to different types of thermal insulations placed in furred assemblies, in which the foil was adjacent to the airspace [9, 12, 13, and 15-18]. The accurate calculations of the airflow and temperature distributions within the test specimens resulted in predictions for the R-values obtained of the present model that were in good agreement with measured R-values (within the uncertainty of the experimental data, see [13, 16, 17, 18] for more details). Furthermore, the model was used to determine the reductions in the R-values of the specimens as a result of increasing the foil emissivity due to water vapour condensation and/or dust accumulation on the surface of the foil.

In a number of previous studies by Saber [24-28], the model was used to conduct numerical simulations to predict the airflow and temperature distributions as well as the R-values of vertical, horizontal and

inclined enclosed airspaces, subjected to different directions of heat flow. The predicted R-values were compared with the R-values for enclosed airspaces of different thicknesses and operating conditions as provided in the ASHRAE handbook of fundamentals [34]. In these same studies the dependence of the R-value on a wide range of the airspace aspect ratio (i.e. ratio of the length or height of the airspace to its thickness) of the enclosed airspace was also investigated. Additionally, practical correlations were developed for determining the R-values of enclosed airspaces of different thicknesses, and for a wide range of values for various parameters, namely, aspect ratio, temperature differential, average temperature, and emissivity of the different surfaces of the airspaces [24-28]. These correlations are ready to be implemented in energy simulations models such as Energy Plus, ESP-r and DOE.

Also, the present model was benchmarked and thereafter used to assess the effect of thermal mass on the thermal performance of Insulated Concrete Form (ICF) wall systems when placed in NRC-Construction's Field Exposure of Walls Facility (FEWF) and subjected to yearly periods of local Canadian climate [10-11, 21-22]. Results showed that the predictions of the present model for the temperature and heat flux distributions within the ICF wall systems were in good agreements with the test data. Recently, the present model was benchmarked against field data obtained in the NRC's FEWF of highly insulated residential wood-frame construction in which Vacuum Insulation Panels (VIPs) were used as the primary insulation components; the results from this work showed that the model predictions were in good agreement with the test data [29-31].

More recently, the hygIRC-C model was benchmarked against test results of a number of samples of Exterior Insulation and Finishing Systems (EIFS) [35]. The test results were obtained using the NRC's Guarded-Hot-Plate (GHP) apparatus in accordance of the ASTM C-177 standard test method [36]. The accurate calculations of the airflow and temperature distribution within the test specimens had resulted that the model predictions for the R-values of different samples were in good agreements with the test results (within ±5%). Thereafter, the present model was used to investigate the effect of air leakage due to infiltration and exfiltration on the effective R-values of different EIFS assemblies, subjected to different climatic conditions. The results of this study will be published at a later date. These studies focused on predicting the thermal performance of different types of walls [1-5, 9-10, 11-13, 15-22, 24-31]; however, no account was made for moisture transport across the wall assemblies.

In instances where the model has been used to account for moisture transport across wall assemblies, the present model predicted the drying rate of a number of wall assemblies shown in Figure 2 and subjected to different outdoor and indoor boundary conditions in which there was a significant vapour drive across the wall assemblies [see [8] for more details). The results showed that there was overall agreement between the results derived from the present model and the hygIRC-2D model, a model that had previously been developed and benchmarked at NRC-Construction [23]. As well, model predictions were in good agreement with the experimental measurements of the drying (Figure 3) and drying rate (Figure 4) of the assembly with respect to the shape of the drying curve and the length of time predicted for drying. Additionally, as shown in Figure 5, the predicted average moisture content of the different wall assemblies over the test periods were in good agreement, all being within ±5% of those measured experimentally [8].

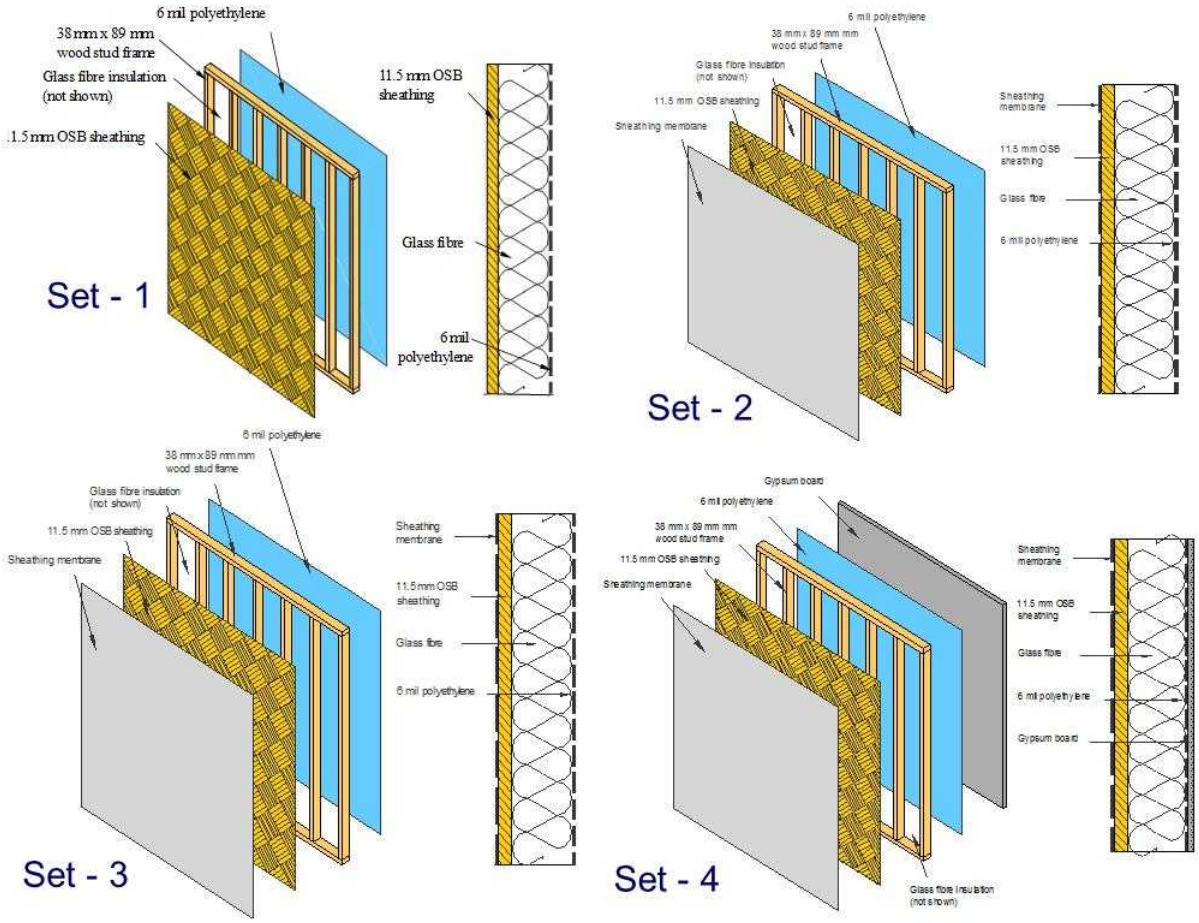


**Figure 2 – Model benchmarking against test results of drying wall assemblies subjected to different outdoor and indoor boundary conditions [8].**

Additionally, with respect to the prediction of the hygrothermal performance of roofing systems, the present model was used to investigate the moisture accumulation and energy performance of reflective (white coloured) and non-reflective (black coloured) roofing systems that were subjected to different climatic conditions of North America [19, 20]. The results of these studies showed that the climatic conditions of St John's and Saskatoon resulted in a high risk of long-term moisture accumulation in the white roofing systems. In case of climatic conditions in which white roofing systems have no risk of moisture accumulation, however, the results of these studies provided the amount of energy saving due to using white roofing systems compared to using black roofing systems (see [19, 20] for more details).

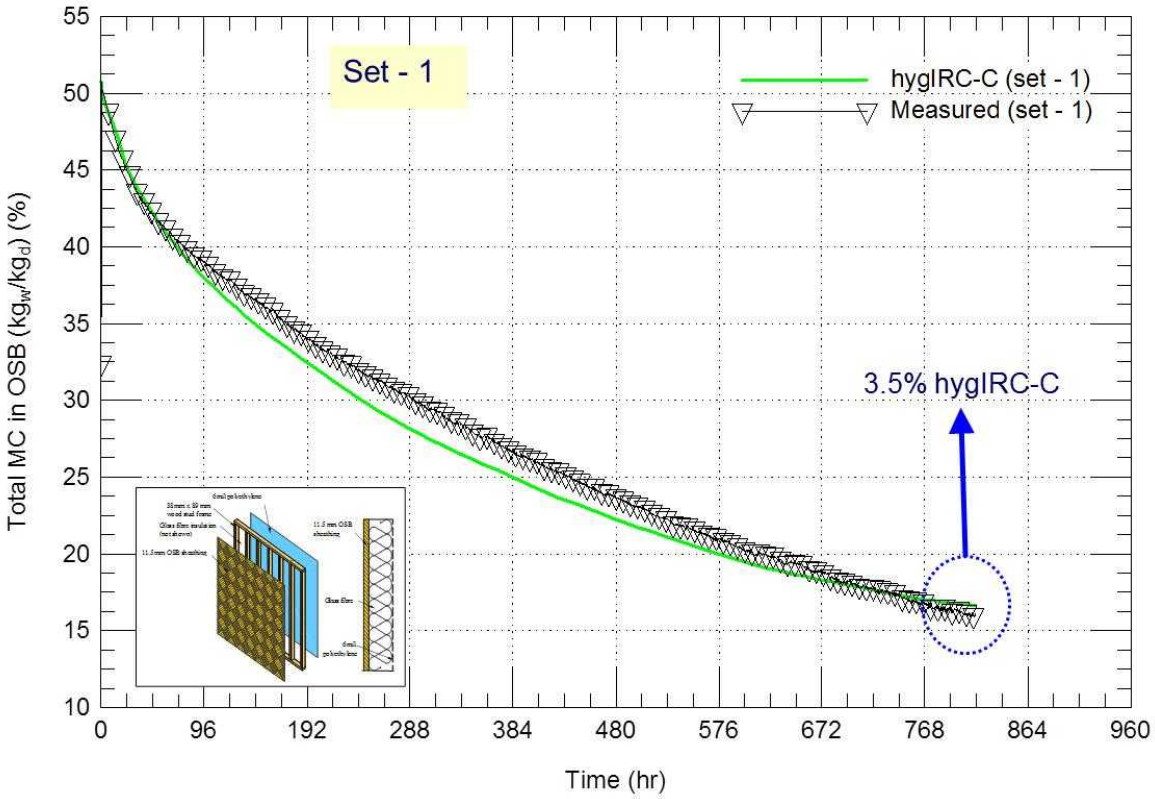


**Figure 3 – Sample results of comparing the predicted and measured moisture content in the OSB layer of set – 1 shown in Figure 2 [8].**

In a recent NRC project, the model was used to address the Code Change Request "CCR-802" to investigate the effect of: (a) air leakage, and (b) adding exterior insulations of different R-values and different water vapour permeance on the risk of condensation and mould growth of different wood-frame wall assemblies with and without structural sheathing, and subjected to different Canadian climatic conditions. The cavity insulation of these wall assemblies was either R-19 or R-24 (see [37 and 38] for more details). The hygrothermal performance criterion that was used in that project was the mould index, which was used in the current project.

Having previously benchmarked the hygIRC-C model to several tests undertaken in field and controlled laboratory conditions, as described above, as well as benchmarking this model against test data of airflow in an airspace and the drying of a stucco plate, as provided in the subsequent sections, this model was used with confidence in this project to predict the hygrothermal performance of different wood frame wall assemblies as well as a steel-stud wall assembly, with different drainage components when these walls were subjected to Canadian climatic conditions.

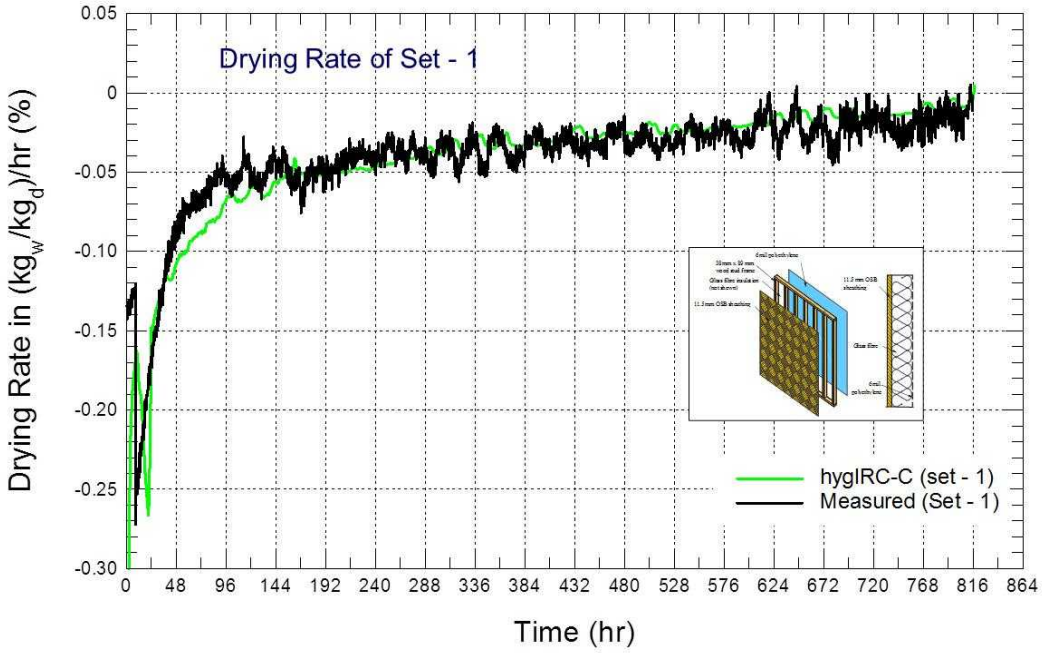


**Figure 4 – Sample results of comparing the predicted and measured draying rate in the OSB layer of set – 1 shown in Figure 2 [8]**

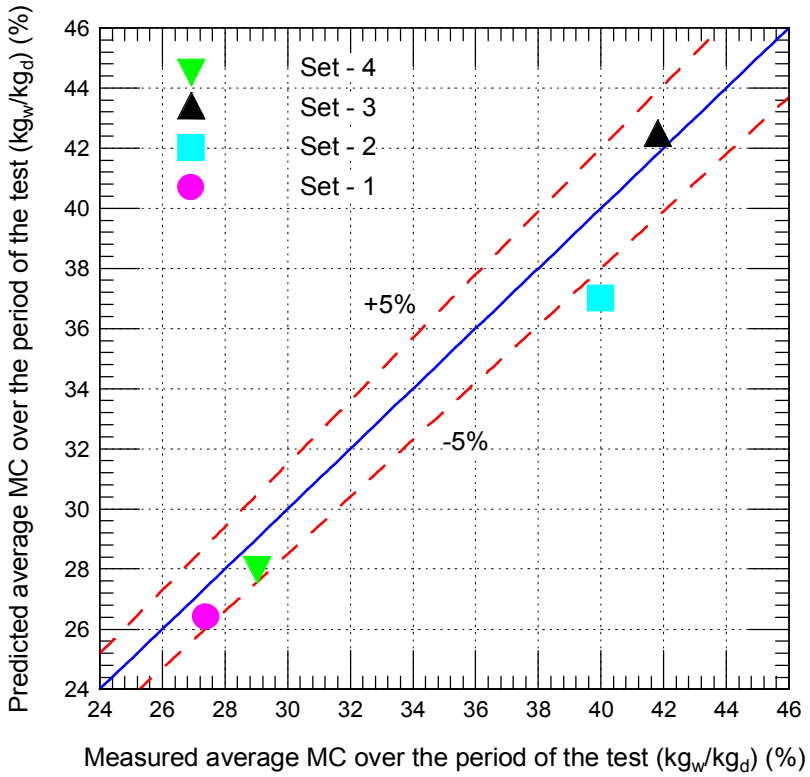


**Figure 5 – Comparison between predicted and measured moisture content in OSB layer over period of test for different wall assemblies (see Figure 2 [8]) subjected to different outdoor and indoor boundary conditions**

# 2.0 Benchmarking of Model against Response of Various Wall Components

The hygrothermal model was benchmarked against the response of three different sets of experimental data to imposed laboratory test conditions, such conditions chosen to permit adequately characterizing the components in respect to a specific physical phenomenon. Each of these components and the related physical phenomena to which the response was sought are provided in Table 1.

**Table 1 – Benchmarking Model to Response of Selected Wall Components**

| Wall Component | Phenomenon & Response Sought | Parameters |
|---|---|---|
| Cavity air space behind cladding | Air velocity as a function of pressure difference between inlet and outlet to cavity | Cavity depths of 10 mm, 20 mm, and 25 mm |
| Non-homogenous highly porous media (drainage components) | Air velocity as a function of pressure difference | |
| Porous media (stucco plate) | Moisture dissipation from stucco plate as a function of time given drying in laboratory conditions | |

In the subsequent sections, and for each of the wall components for which the model was benchmarked to the response derived from experimental tests, a rationale is provided for completing the benchmarking exercise, a brief summary of the experimental set-up is provided, and the results from the tests are compared to those derived from simulation.

## 2.1 Cavity Air Space behind Cladding - Airflow Test Data

The need to characterize the air velocities in cavities providing an air space behind cladding arises because such flow, or lack of flow, would affect the process of moisture dissipation from the cavity that in turn affects moisture accumulation in porous wall components such as stucco and wood. The expectation being that less moisture would be retained in ventilated as compared to vented cavities as ventilated cavities having both an inlet and outlet, allow the flow of air through the air space. Since vented cavities of wall assemblies have only one opening at the base of the wall, the flow of air is necessarily more restricted and may be dominated by natural convective effects that arise due to temperature differences that occur across the cavity and the natural buoyancy of air. The rate of flow for a given cavity depth and pressure difference across the inlet to and outlet from the cavity, would determine the amount of moisture that could be drawn from the cavity.

In this section, information is provided on the benchmarking of the hygIRC-C model against experimental data of airflow in an air space of different depth and subjected to different pressure differences; the different cavity depths investigated are given in Table 1.

### 2.1.1 Description of Test Apparatus and Test-set up

The test apparatus for benchmarking the model against experimental data for forced airflow in cavities is shown in Figure 6. It consists of an air pump that is used to generate forced air flow thought the cavity by applying a pressure at the inlet portion of the apparatus. The cavity is formed by two parallel plates (ca. 12 mm thick) of acrylic plastic of nominal width 400 mm and height 2000 mm. The distance between the plates, and hence the cavity depth, can be changed with the use of purposely fabricated metal spacers having sizes of 10 mm, 20 mmm and 25 mm. As well, the size of the spacer can be made to be the same depth as a drainage component to permit measuring the component's air permeability. Openings have been made along the inlet and outlet chutes as well as mid-height along the length of the parallel plates to accommodate air velocity sensors (Omnidirectional hot wire anemometers) such that velocities can be acquired over the course of a test sequence. As can be seen in Figure 7, three sensors were used across the chute at the inlet or outlet or across the width of the generic wall cavity apparatus. The velocity sensors are equidistant from one another, and as well, can be adjusted to acquire data at different depths across a cavity such that the air velocity profile at these locations can readily be acquired. As well, pressure sensors were located in line with the air velocity sensors at both the inlet and outlet portions of the wall and from which the pressure difference between the inlet and outlet could be determined. The temperature and relative humidity of the air were also measured such that proper flow measurements could be calibrated in relation to the velocities acquired during the test sequence.

A more detailed description of the apparatus is provided in the Task 4 report (Appendix 1) as is information on the calibration of the apparatus.

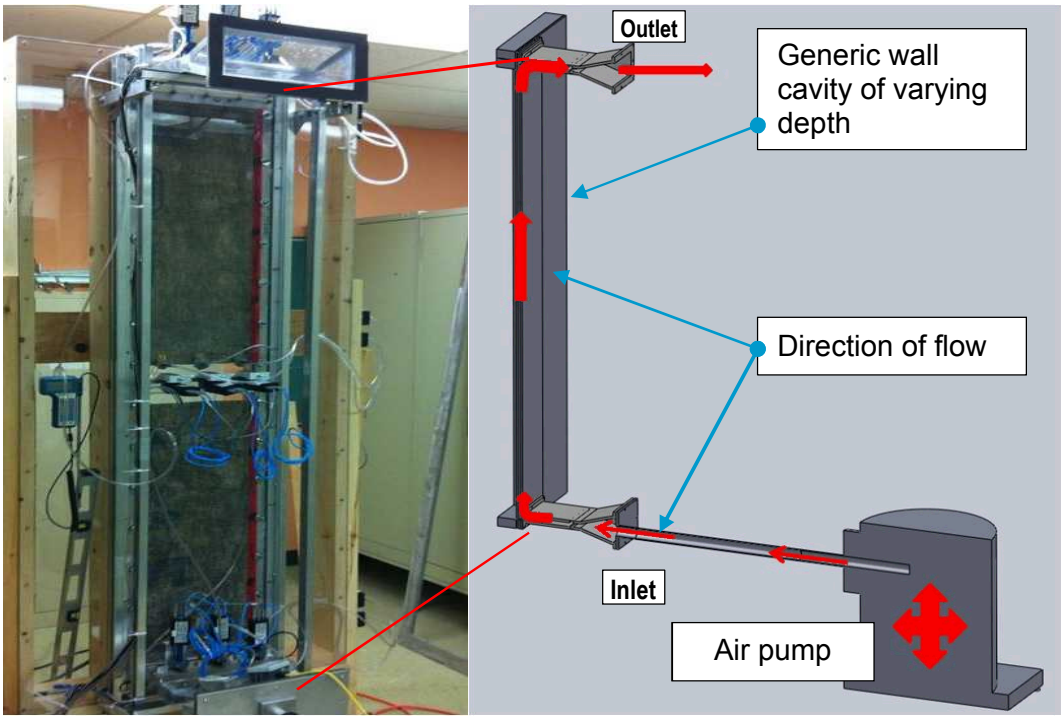


**Figure 6 – Test apparatus for model benchmarking of forced airflow in cavities to determine air permeability of non-homogenous and highly permeable porous materials**

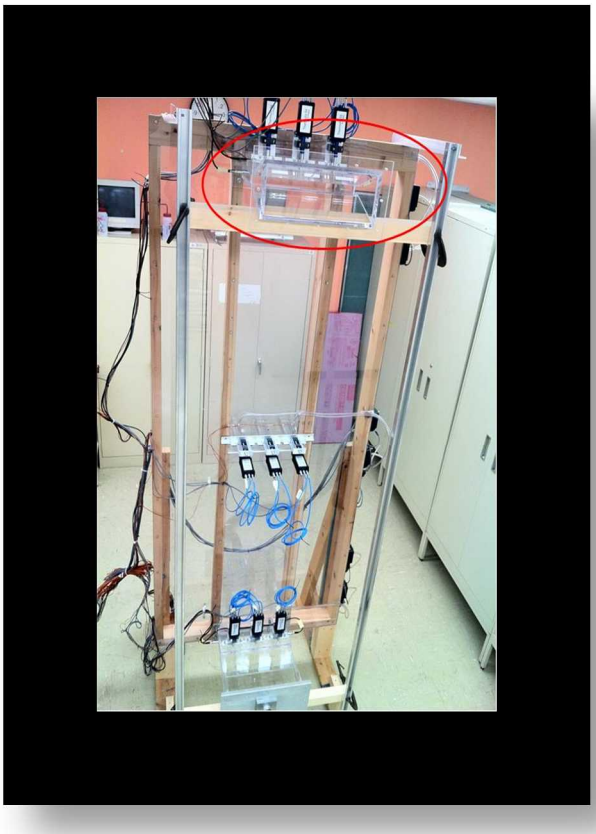

**Figure 7 - Generic wall cavity apparatus showing location of air velocity sensors**

### 2.1.2 Testing Schedule

Testing consisted of acquiring air velocity data at selected pressure levels across the width of the inlet and outlet chutes and the width of the apparatus at its mid-height, as shown in Figure 7. Air velocity measurements were also taken in the depth of the cavity at each control location. The pressure levels used to generate the air flows for the selected cavity depths of 10mm, 20mm and 25 mm are given in Table 2.

**Table 2 – List of air velocity measurements acquired at different conditions and cavity depths**

| Pressure difference ΔP for 10 mm | Pressure difference ΔP for 20 mm | Pressure difference ΔP for 25 mm |
|---|---|---|
| 5.0 Pa ± 1.0 Pa | 1.3 Pa ± 0.26 Pa | 0.84 Pa ± 0.21 Pa |
| 10.0 Pa ± 1.0 Pa | 2.6 Pa ± 0.26 Pa | 1.68 Pa ± 0.21 Pa |
| 15.0 Pa ± 1.0 Pa | 3.9 Pa ± 0.26 Pa | 2.52 Pa ± 0.21 Pa |
| 20.0 Pa ± 1.0 Pa | 5.2 Pa ± 0.26 Pa | 3.36 Pa ± 0.21 Pa |
| 25.0 Pa ± 1.0 Pa | 6.5 Pa ± 0.26 Pa | 4.2 Pa ± 0.21 Pa |

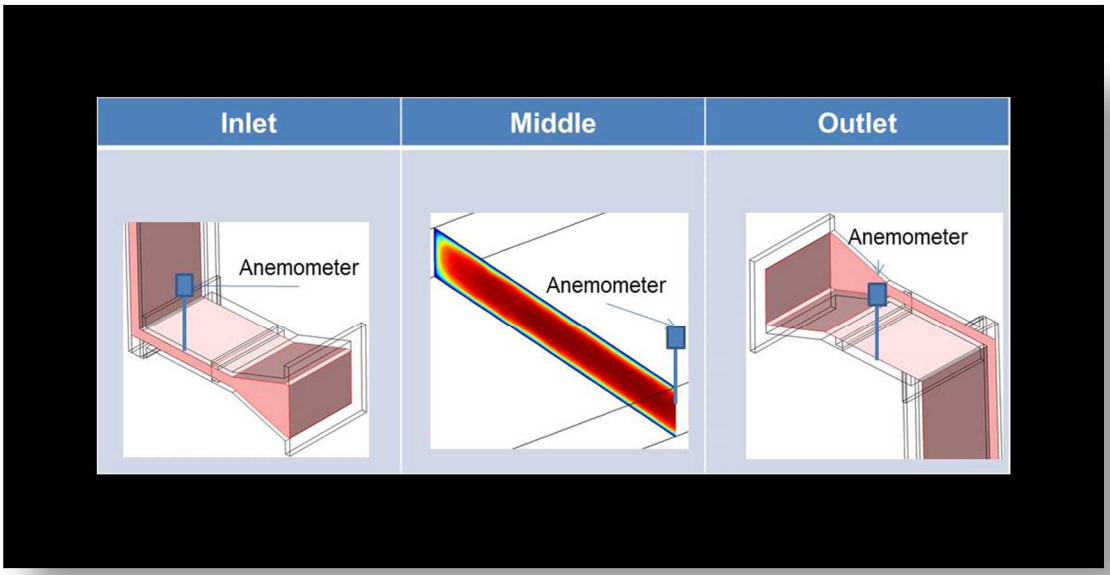


**Figure 8 – Locations at which model predictions and measurements of airflow were compared**

### 2.1.3 Use of Simulation Results to Derive Air velocity Profiles at Control Locations

Selected results from simulation are depicted graphically in Figure 9 to Figure 11. In Figure 9 is shown the simulation results for the inlet and outlet chutes along the length of the respective chutes and in which can be seen the spatial distribution of air velocity values ranging from null to ~ 2.5 m/s. The results provided in the graphic suggest that the air velocities increase to about 1 m/s along the length of the inlet chute and likewise decrease at the outlet chute, although for the latter case, the variations in velocity in the depth of the chute are more pronounced as compared to the corresponding sections of the inlet chute.

A graphical depiction of simulation results in a "horizontal" plane showing spatial distribution of air velocity along length of cavity air flow characterization apparatus is given in Figure 10. The values of air velocity range from null to ~ 2.9 m/s. In the sectional view the distribution of velocities in the depth of the cavity are apparent and suggest that velocities at the mid-height of the cavity air flow characterization apparatus along the length of the cavity are > 2.5 m/s.

Given that the spatial distribution of air velocities within the cavity at any section are known from the results of simulation, these results can then then plotted at different driving pressures ($\Delta P$) such that they can be compared to results from measurements obtained experimentally.

Such comparisons are shown in Figure 11 in which the simulation results are provided at three simulated pressure differences at control sections located at inlet, outlet and mid-height of cavity air flow characterization apparatus. The air velocities are given in relation to the depth of the cavity. The experimental data, complete with error bars, is also plotted such that a comparison can be made between the results derived through simulation and those obtained from experiment.

Using this same approach, the results from several tests were used to compare to those derived through simulation as is described in the subsequent sections.

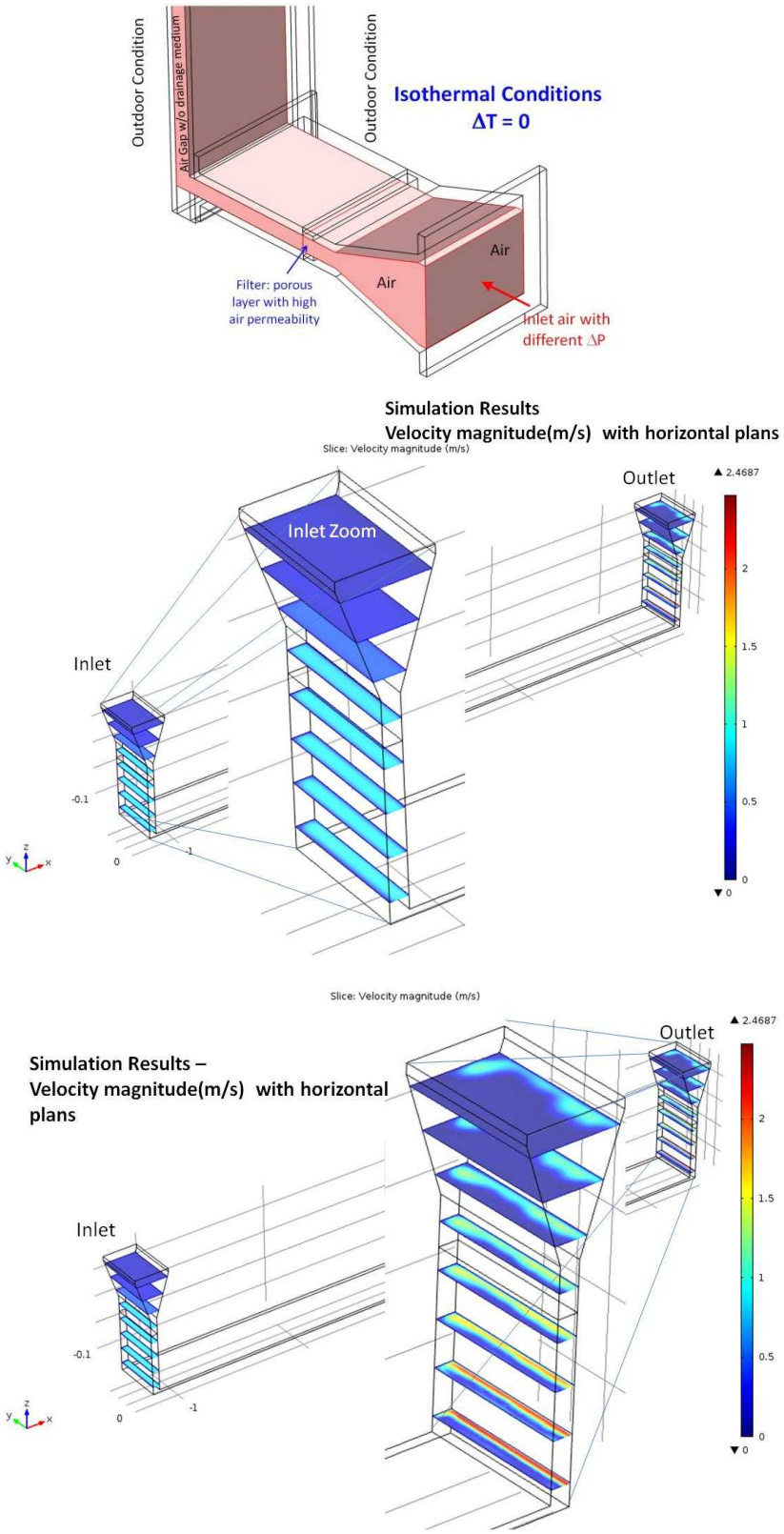


**Figure 9 – Graphical depiction of simulation results showing the spatial distribution of air velocity in the inlet and outlet chutes for selected sections; range of velocities 0 to ~ 2.5 m/s**

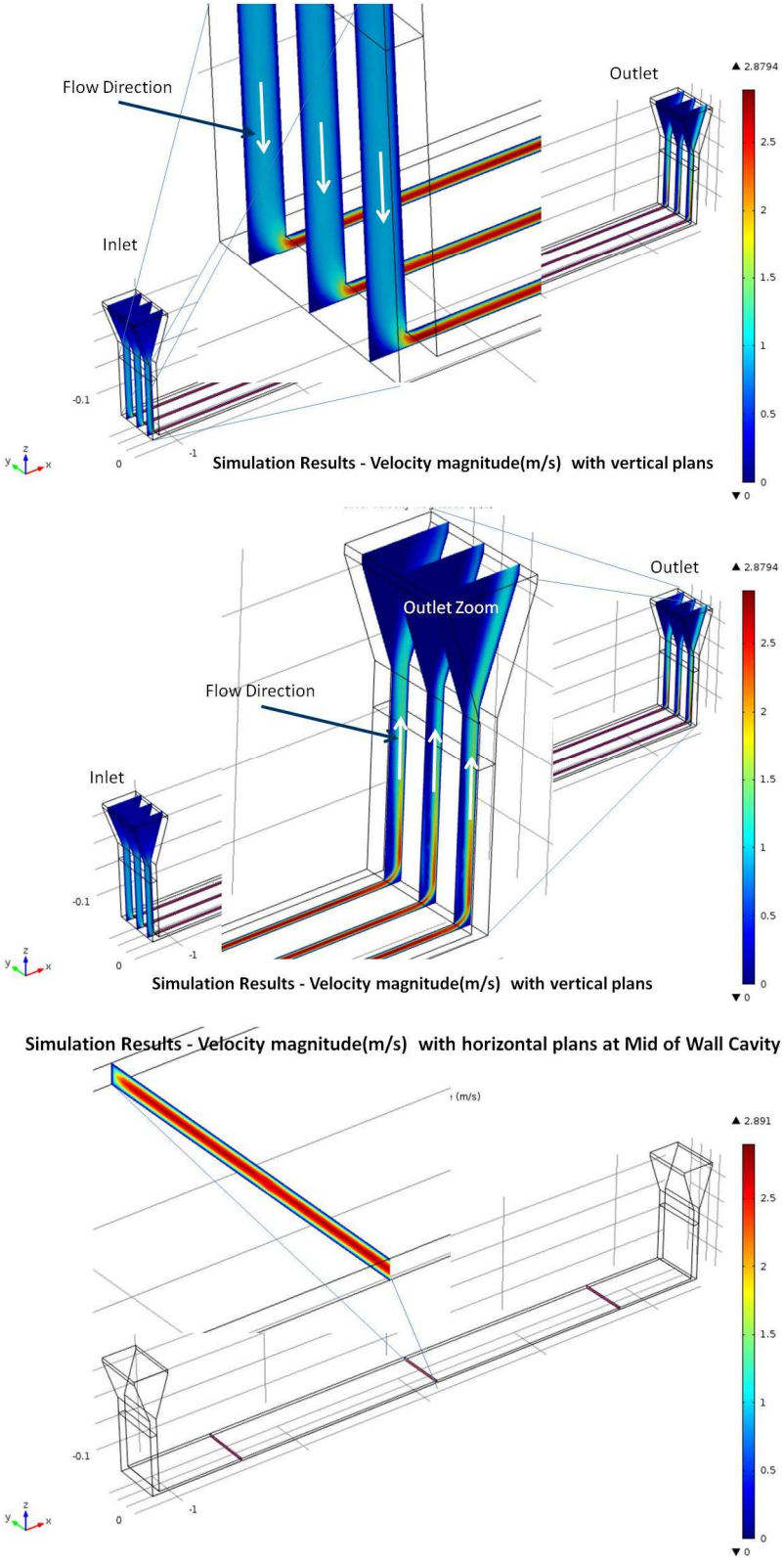


**Figure 10 – Graphical depiction of simulation results in a "horizontal" plane showing spatial distribution of air velocity along length of air flow characterization apparatus; sectional view shows distribution in the depth of the cavity; range of velocities 0 to ~ 2.9 m/s**

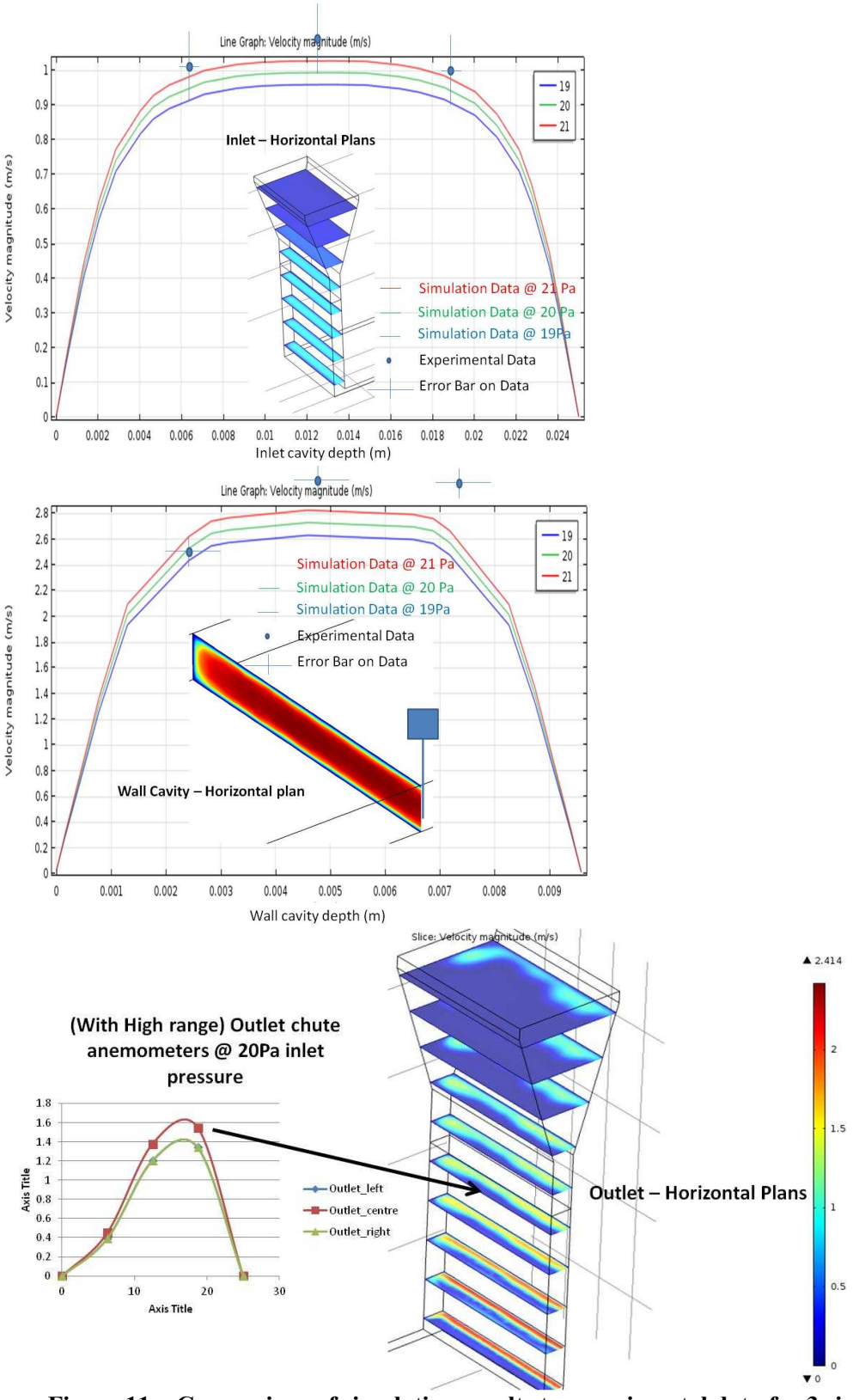


**Figure 11 – Comparison of simulation results to experimental data for 3 simulated pressure differences at control sections located at inlet, outlet and mid-height of cavity air flow characterization apparatus; air velocities are given in relation to the depth of cavity**

### 2.1.4 Comparison of Test Results to Those Derived from Simulation

Selected test results for air velocity measurements as compared to those derived from simulation for the 10 mm cavity depth are given in Figure 12 and Figure 13, those for 20 mm cavity depth in Figure 14 and Figure 15, and those for 25 mm cavity depth in Figure 16 and Figure 17; the remaining tests results for cavity air velocity measurements for respective depths of 10, 20 and 25 mm are provided in Appendix 2.

Typically, in each figure a set of three air velocity (m/s) plots are given, the left-most plot on the page for the inlet section, thereafter the middle section located the mid-height of the cavity wall, and the third and right-most plot for the outlet section. The velocity profiles (m/s) obtained from tests at the specified pressure differences, are plotted as individual points that also includes the error band. Those derived from simulation are those plotted at specific pressure differences as solid lines.

For example, in Figure 14 (cavity depth 20 mm), the resultant velocity profiles derived from simulation occur at a pressure difference of 1.3 Pa ± 0.26 Pa, or as shown in Figure 15, at 2.6 Pa; each of these profiles was plotted as derived from simulation and in which one can also discern the plot of individual values of air velocity, as measured in the test, together with their associated error bands. For example, in the plot shown in Figure 14 for the inlet location, a data point for air velocity is evident at an arc length of ~0.018 m having a value of 0.55 ± 0.1 m/s. In this same plot, it is evident that each of the measurement points for air velocity fall within the margin of error associated with the results derived from simulation.

#### *2.1.4a. — Air velocity profile of 10 mm cavity depth*

Results of air velocity profiles and measurements for a 10 mm cavity depth obtained for five pressure levels (i.e. 5.0, 10.0, 15.0, 20.0, 25.0 Pa ± 1.0 Pa) are shown in Figure 12 ($\Delta P$ = 5 Pa) and Figure 13 ($\Delta P$ = 10 Pa) and in Appendix 2 in Figure 35 ($\Delta P$ = 15 Pa), Figure 36 ($\Delta P$ = 20Pa) and Figure 37 ($\Delta P$ = 25 Pa). Of the total of 45 data points shown in the plots, 12 data points were not consistent with simulation results.

#### *2.1.4b. — Air velocity profile of 20 mm cavity depth*

A review of all available plots for this cavity depth and for which tests were undertaken at five pressure levels (i.e. 1.3, 2.6, 3.9, 5.2, 6.5 Pa ± 0.26 Pa) indicated that of the total of 45 data points shown in the plots, only 5 of the measured data fell outside of the plots of air velocity derived from simulation.

#### *2.1.4c. — Air velocity profile of 25 mm cavity depth*

As regards the air velocity profiles for the 25 mm cavity depth, the results at five pressure levels (i.e. 0.84, 1.68, 2.52, 3.36, 4.2 Pa ± 0.21 Pa) are shown in Figure 16 and Figure 17 and in Appendix 2 in Figure 41, Figure 42 and Figure 43. Some measured data fell outside the plots for air velocity derived from simulation in the following instances: (i) at a $\Delta P$ = 1.68 Pa (Figure 17) for the middle section at an arc length of ~0.03 m; (ii) at a $\Delta P$ = 2.52 Pa (Figure 41) for the middle section, at an arc length of ~0.03 m; at (iii) $\Delta P$ = 2.52 Pa (Figure 41) at an arc length of ~ 0.018 m and (iv) 4.20 Pa (Figure 43) for the outlet section, at an arc length of ~0.018 m. Thus only 5 data points were not consistent with simulation results of a total of 45 data points.

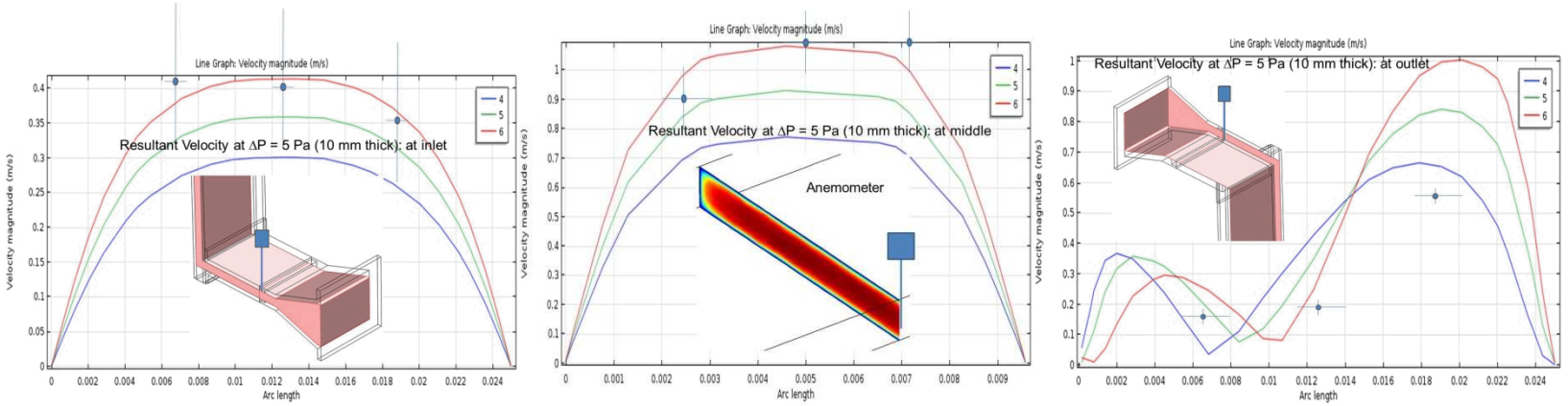


**Figure 12 – Comparison of velocity measurements for an airspace of 10 mm depth with test data at the inlet, middle and outlet of the airspace at ΔP = 5.0 Pa ± 1.0 Pa**

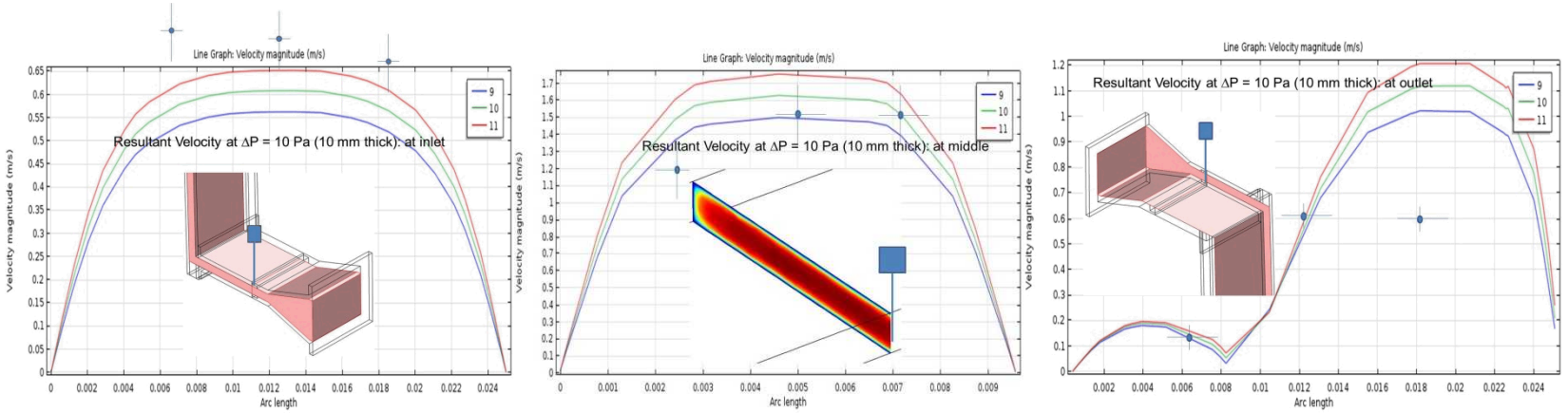


**Figure 13 – Comparison of velocity measurements for an airspace of 10 mm depth with test data at the inlet, middle and outlet of the airspace at ΔP = 10.0 Pa ± 1.0 Pa**

| Inlet location | Middle cavity location | Outlet location |
|---|---|---|

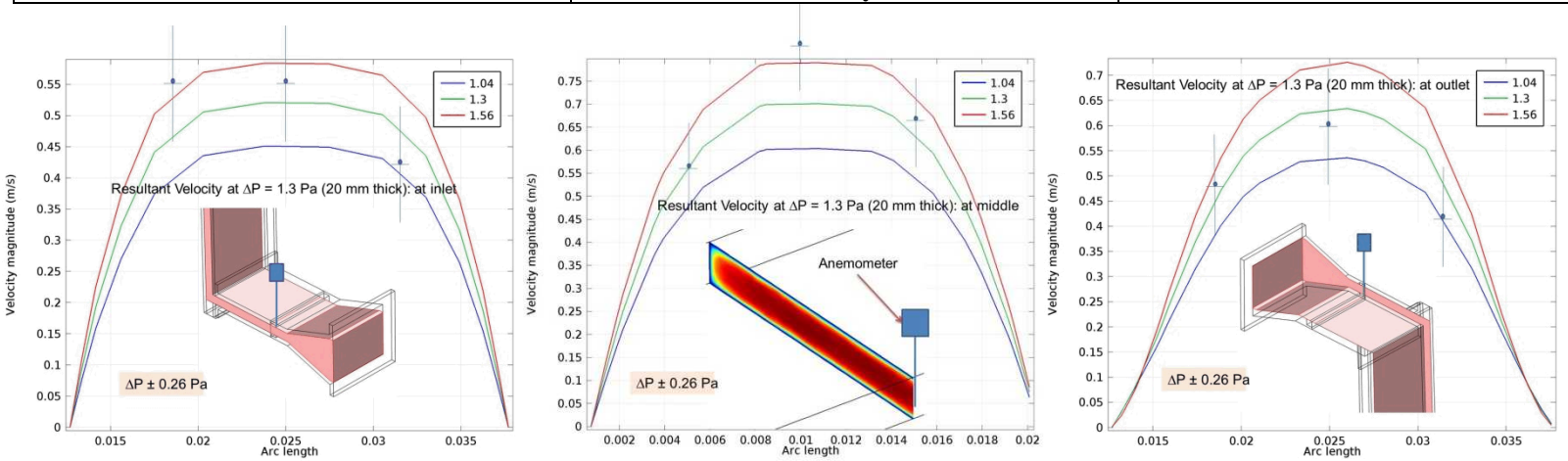


**Figure 14 – Comparison of velocity measurements with test data at given location for airspace of 20 mm depth at ΔP = 1.3 Pa ± 0.26 Pa**

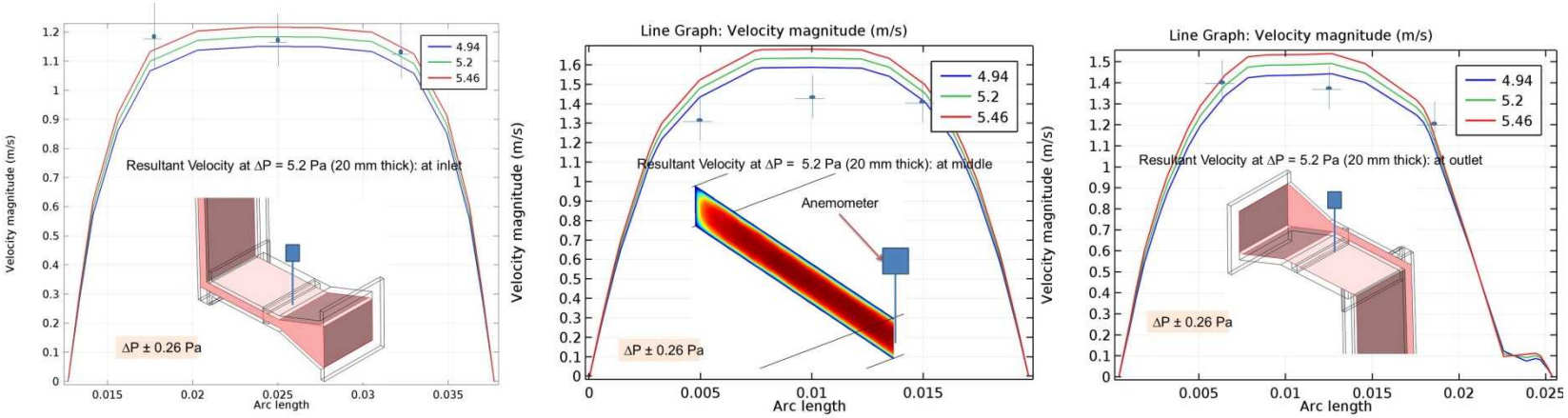


**Figure 15 – Comparison of velocity measurements with test data at given location for airspace of 20 mm depth at ΔP = 2.6 Pa ± 0.26 Pa**

| Inlet location | Middle cavity location | Outlet location |
|---|---|---|

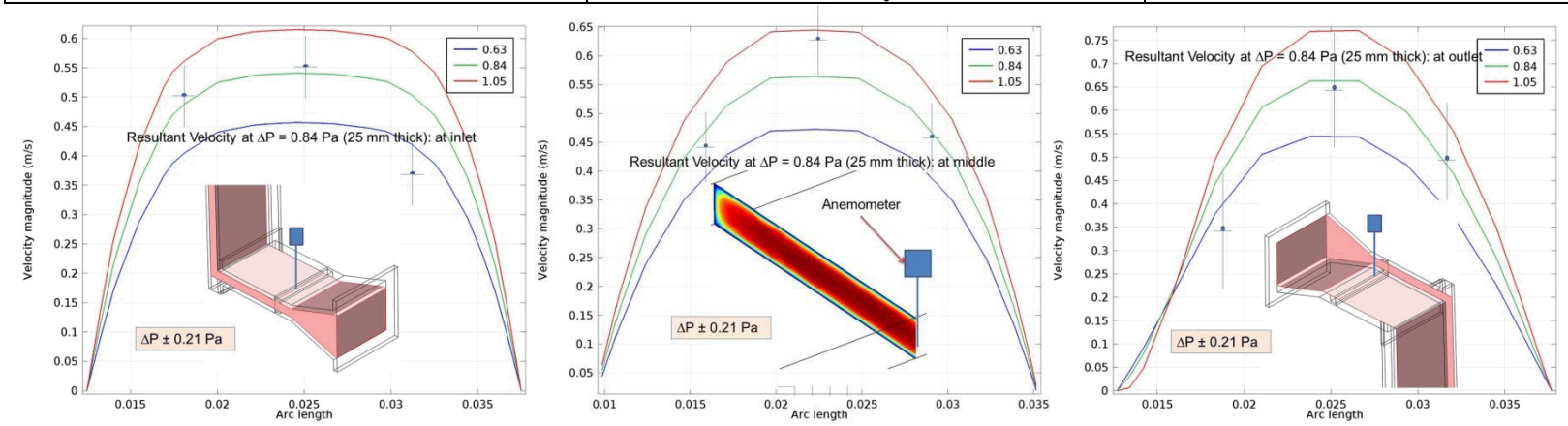


**Figure 16 – Comparison of velocity measurements for an airspace of 25 mm depth with test data at the inlet, middle and outlet of the airspace at ΔP = 0.84 Pa ± 0.21 Pa**

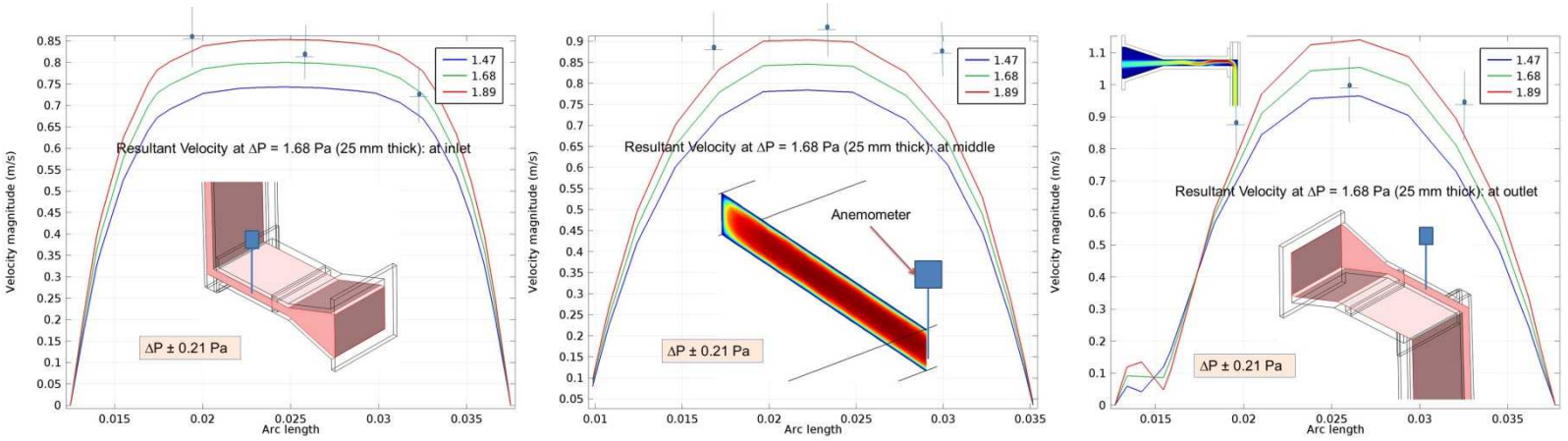


**Figure 17 – Comparison of velocity measurements for an airspace of 25 mm depth with test data at the inlet and middle of the airspace at ΔP = 1.68 Pa ± 0.21 Pa**

### 2.1.5 Derivation of Flow Rates in Cavity Air Spaces from Simulation Model

On the basis of these results, and as shown in Figure 18, the model simulation provided an estimate of the volumetric flow rate as a function of pressure differential across openings to the air space for different cavity depths. These simulation results were subsequently used to determine the effective permeability of different drainage components as is discussed in the subsequent section.

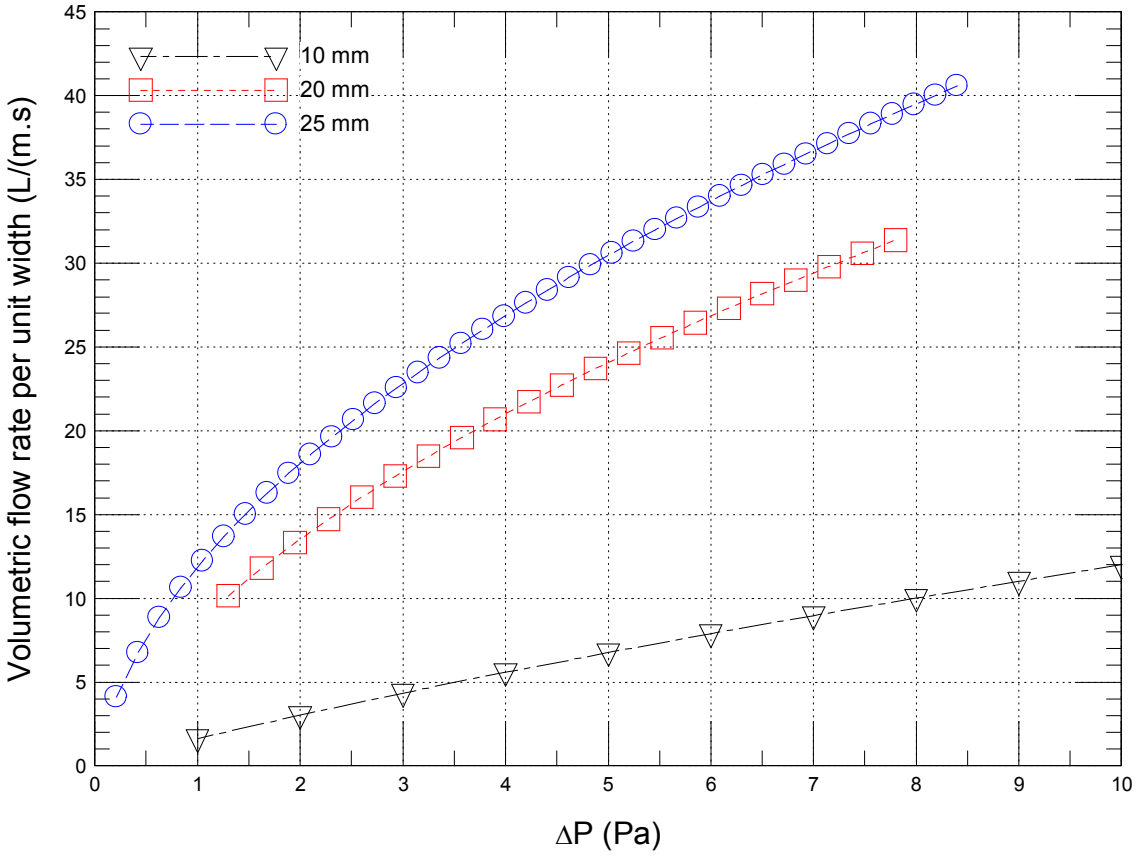


**Figure 18 – Dependence of cavity airflow rate on pressure deferential for airspace of different thickness**

## 2.2 Airflow in Non-homogenous Highly Porous Media

In the previous section a description was provided for the characterization of air flow in unobstructed cavities for cavity sizes ranging between 10 and 25 mm in depth and consistent with cavity sizes typically found in wall assemblies constructed according to the minimum requirements set out in Part 9 of the NBCC. Of interest, as well, is knowledge of how air flow in wall cavities behind cladding may be altered with the incorporation of a drainage component in the construction of the assembly as compared to the unobstructed cavity. Given the many different types of drainage components of interest to this project, it was necessary to determine whether the presence of a drainage component significantly hindered or aided the flow of air in this air space.

### 2.2.1 Air Permeability Tests: Principle and procedures

The permeability to air of the drainage components was determined using accepted methods of determining permeability that are used for less porous materials such as flexible sheet or rigid panel-type materials. More specifically, the specimens were initially tested according to the same procedure used for all of the air permeability testing conducted as described by Kumaran and Bomberg [39].

#### *2.2.1a — Basis for air permeability tests*

The method assumes a unidirectional steady laminar flow of air through a porous media of thickness L, from a region of pressure $P_a$ to one of pressure $P_b$ as represented in Figure 19. From Darcy's law for flow in porous media:

$$\frac{Q}{A} = u_a = \frac{\kappa_a}{\mu_a} \cdot \nabla P = \frac{\kappa_a}{\mu_a} \cdot \frac{\Delta P}{L} \qquad \text{Eq. (1)}$$

Where:

Q = volumetric flow rate of air ($m^3\ s^{-1}$),
A = normal cross-sectional area of the material ($m^2$),
u = average flow velocity ($m\ s^{-1}$)
$\kappa_a$ = intrinsic air permeability of the material ($m^2$),
$\mu_a$ = absolute viscosity of air ($1.835 \times 10^{-5}$ Pa•s at 23°C at which the tests for different drainage mediums were conducted),
$\Delta P$ = difference in "piezometric pressure" of air across the material (Pa)

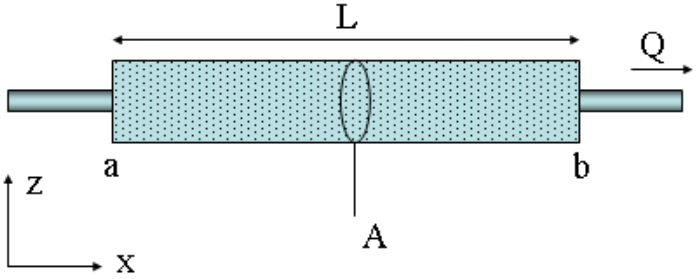


**Figure 19 – Unidirectional steady laminar flow (Q) through porous media of length L and area, A**

Equation (1) is applicable to homogeneous and non- homogeneous materials and membranes (e.g. plywood, OSB, XPS, EPS). The air flow resistance (R) of the specimen can be defined as:

$$R = \frac{\mu_a}{\kappa_a} \cdot L \qquad \text{Eq. (2)}$$

From equations (1) and (2)

$$R = \frac{(\Delta P \cdot A)}{Q \cdot \mu_a} \quad \text{Eq. (3)}$$

It is also useful to define the air permeance ($K_a$) as:

$$\frac{1}{R} = K_a = \frac{\kappa_a}{L} \quad \text{Eq. (4)}$$

From Equations 1 and 4:

$$K_a = \frac{Q \cdot \mu_a}{\Delta P \cdot A} \quad \text{Eq. (5)}$$

The air permeability ($\kappa_a$) of the specimen can be defined as the air permeance ($K_a$) multiplied by the thickness (L) or:

$$\kappa_a = \frac{Q \cdot L \cdot \mu_a}{\Delta P \cdot A} \quad \text{Eq. (6)}$$

Thus measurements of Q, ΔP and A may be used to evaluate R, the air resistance as well as air permeance and air permeability of the material. The air flow characteristic determined will be an average property of the material for the metering area and so the material need not be homogeneous or of uniform thickness.

***2.2.1b — Test Set-up***

In the current project, the experimental setup shown in Figure 20 was used for the determination of air flow resistance of drainage components. Compressed dry air from a cylinder was admitted to the test chamber from the pressure regulating valve. This air flowed through the porous specimen which was open to the atmosphere. Consequently an appropriate steady state was maintained in the assembly; different steady states being achieved by changing the air pressure in the chamber. The steady state flow rate (Q) in equation (5, 6) was measured by a mass flow controller (MKS 1179A 24CS1 BV; 20000 STD $cm^3min^{-1}$; resolution: 0.1% of F.S; accuracy: ±1.0% of F.S.) connected between the pressure regulating valve and the chamber. The air pressure difference across the specimen was measured by using a differential pressure transducer. One of two transducers were used for any given test; one used at a higher pressure range of 1000 Pa (MKS Model 223B D 00010 AAB; range: 1000 Pa; accuracy: ±0.5% of F.S / ±5 Pa); and the other for lower ranges that did not exceed 250 Pa (Setra Model 264-1-001WD-2D-T1-E; range: 0-250 Pa; accuracy: ±0.4% FS; ± 1 Pa).

***2.2.1c — Test Procedure***

Measurement under steady state conditions is sufficient to determine the ratio (ΔP / Q) and was determined by measuring ΔP as a function of Q. The slope (ΔP/Q) in equation (3) was determined in each case. The following test procedure for evaluating the air flow resistance of materials was specified:

(1) Five specimens were tested and the average of five results reported as air flow resistance of the material;
(2) At least four data pairs were used to calculate the air flow resistance;
(3) As appropriate for any specimen, pressure differences ranging between 1 and 1200 Pa and air flow rates ranging between 20 and 900 $cm^3min^{-1}$ were used.

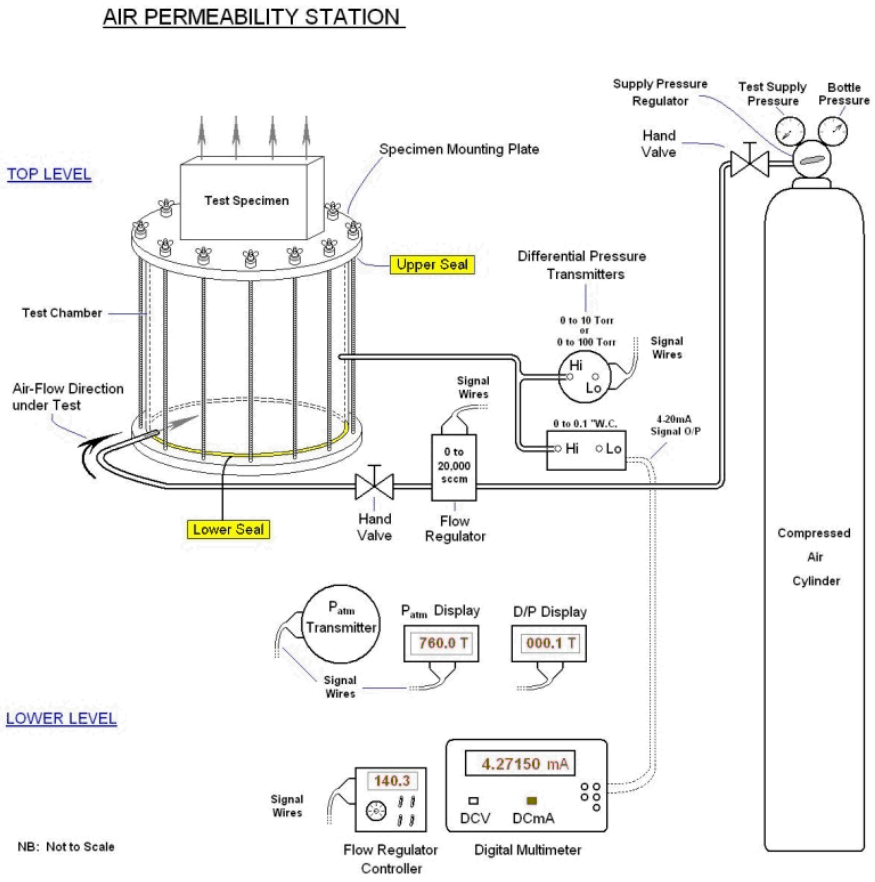


**Figure 20 – Air permeability test set-up**

### 2.2.2 Drainage Components - Air Permeability Test Results

To quantify the air flow in the drainage components and to examine the effects of the height of the component on experimental results, four component lengths were tested; these were: 14.3 cm; 28.5 cm; 42.8 cm; and 57.0 cm. The results from these tests are given in the Task 2 report (see Appendix 1 for the list of project reports). Provided in Table 3 are the results obtained for the drainage component of Client C; a photo the open matrix Nylon mesh mat is shown in Figure 21. Values of air permeability and permeance are provided in relation to the length of the test specimen (height) and flow direction, the respective directions being shown in Figure 21. The average values in the X- and Y-directions are provided as are the average values for the X- and Y-directions combined and values for the air permeability coefficient ($\kappa_a$). The variation in values of air permeability coefficient for given orientations in relation to the average value in the X- and Y-directions is given in Table 4.

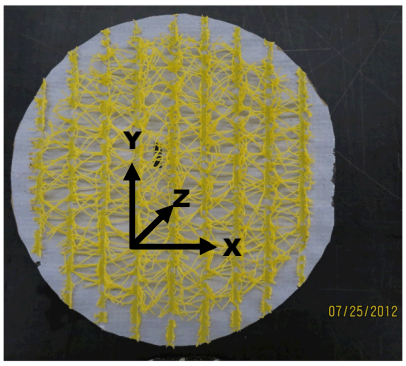


**Figure 21 – Open matrix Nylon mesh bonded to nonwoven sheathing membrane**

**Table 3 – Air Permeability and Permeance of open matrix Nylon mesh bonded to nonwoven sheathing membrane**

| Mesh Orientation | Height m | Permeability $l \cdot (75\ Pa)^{-1} \cdot m^{-1} \cdot s^{-1}$ | Permeance $l \cdot (75\ Pa)^{-1} \cdot m^{-2} \cdot s^{-1}$ | Permeability coefficient (κ) $m^2$ |
|---|---|---|---|---|
| Y-direction | 0.143 | 7.492E+03 | 5.239E+04 | 1.698E-06 |
| | 0.285 | 8.405E+03 | 2.949E+04 | 1.905E-06 |
| | 0.428 | 1.231E+04 | 2.875E+04 | 2.790E-06 |
| | 0.570 | 9.676E+03 | 1.698E+04 | 2.193E-06 |
| Average Y | | 9.471E+03 ($\sigma_n$=1.8E+03) | 3.190E+03 ($\sigma_n$=1.3E+03) | 2.147E-06 ($\sigma_n$=0.41E-06) |
| X-direction | 0.143 | 3.669E+03 | 2.565E+04 | 8.316E-07 |
| | 0.285 | 4.216E+03 | 1.479E+04 | 9.556E-07 |
| | 0.428 | 3.765E+03 | 8.796E+03 | 8.533E-07 |
| | 0.570 | 4.608E+03 | 8.085E+03 | 1.044E-06 |
| Average X | | 4.065E+03 ($\sigma_n$=0.38E+03) | 1.433E+04 ($\sigma_n$=0.70E+03) | 9.213E-07 ($\sigma_n$=0.85E-07) |
| Average X & Y | | 6.768E+03 | 2.311E+03 | 1.534E-06 |
| Z-direction | 0.011 | 7.489E-03 | 7.103E-01 | 1.698E-12 |

**Table 4 – Variation in Values of Permeability coefficient (κ) for given Orientation in Relation to Average in X and Y-directions**

| Orientation | Permeability coefficient (κ) $m^2$ | Dev. (%)* |
|---|---|---|
| Average Y-direction | 2.147E-06 ($\sigma_n$=0.41E-06; $\sigma_n / \bar{x}$ = ~20%) | 40 |
| Average X-direction | 0.9213E-06 ($\sigma_n$=0.085E-06; $\sigma_n / \bar{x}$ = ~9%) | -40 |
| Average X and Y-direction | 1.534E-06 | - |

* Deviation from average in X and Y-direction

As is shown in Table 4, there is a marked difference in value for the permeability coefficient ($\kappa_a$) in both the X and Y direction in relation to the average of both the X- and Z-directions. This is entirely expected given that the mesh has an orientation that allows greater flow in the Y- as compared to the X-direction. The X-, Y- and Z- directions are shown in Figure 21. When completing the 2-D simulation (see Task 6 report; Appendix 1), which was undertaken in the Y- and Z-directions, an issue then arose as to what value for permeability coefficient should be used given that the mesh orientation was in the Y-direction, but air flow may nonetheless traverse across the mesh in both the X- and Y-directions. This is addressed in the subsequent sections.

### 2.2.3 Dependence of air permeability coefficient on pressure differential

An investigation was conducted to determine the air flow rates generated in the air cavity incorporating, or not, a drainage component and the sensitivity of the air flow rates to variations in air permeability coefficient ($\kappa_a$) and pressure difference; results of this investigation are given in Figure 22 to Figure 25.

In Figure 22 is shown a comparison of air flow rate of a 10.5 mm deep cavity, with and without drainage medium (drainage component; Figure 21) as derived from simulation and using the value of the average air permeability coefficient in the Y-direction (i.e. $\kappa_a = 2.15 \times 10^{-6}$ m$^2$). Clearly, the presence of the drainage medium reduces the cavity air flow rate. The sensitivity of the cavity air flow rate to variations in value of the air permeability coefficient ($\kappa_a$) of ± 50% in relation to the average $\kappa$ in Y-direction value is given in Figure 23. Necessarily, the flow will either increase or diminish in relation to the corresponding changes in value of the air permeability coefficient.

Variations in volumetric flow rate in the cavity will also vary, not only in relation to the value of the air permeability coefficient, but also in relation to the pressure difference that drives the flow; this relation is shown in Figure 24, in which the values for the air permeability coefficient range between 0.1 and 2 times the average value in the Y-direction for pressures differences of 20, 50 and 75 Pa. The value of the effective permeability is given as the product of the dynamic permeability factor (F) and the average value of the air permeability coefficient ($\kappa_a$) in the Y-direction. This relation is of importance because it suggests that a specific value of the air permeability coefficient ($\kappa_a$) can be determined for given values of pressure difference that directly correspond to the air flow rates obtained from experiment.

Accordingly, a comparison was made between the measured volumetric air flow rate (Q) and that predicted by simulation at different $\Delta$P's, i.e., for values of $\Delta$P of 5, 10, 15 and 20 Pa. The values derived from simulation at the given $\Delta$P's are shown in Figure 25 and those from experiment, in Figure 26 for values of $\Delta$P of 5 and 10 Pa, and Figure 27 for values of $\Delta$P of 15 and 20 Pa; values for $\kappa_a$ in the X-, and Y-directions and the average value for $\kappa_a$ are provided in the adjoining tables of these respective figures.

Using the drainage medium shown in Figure 21 as example, the values for air flow rate in the cavity that arise due to $\Delta$P's of 5 and 10 Pa (Figure 26), as compared to that derived from simulation most closely match the values obtained experimentally when the maximum value for the air permeability coefficient ($\kappa_{a,max}$) is assumed as compared to either the minimum or average value; comparing values of air flow from the simulated to that from experiment, a deviation of -1.2 % and ~ +12% is evident at respective $\Delta$P's of 5 and 10 Pa. Whereas for $\Delta$P's of 15 and 20 Pa and when an average value for $\kappa_a$ is assumed, the respective deviations are +2.4% and +7.7% from simulated to that of experiment. Thus the deviations from experiment can be minimized provided the assumed value for $\kappa_a$ is selected in relation to the $\Delta$P acting along the length of the cavity incorporating the drainage media. This suggests that $\kappa_a$ is pressure dependent and this is a reasonable assumption given that for the range of $\Delta$P's to which the different media were evaluated, the airflow that arise are not likely laminar but turbulent and this may be captured by varying the value of $\kappa_a$ as a function of $\Delta$P.

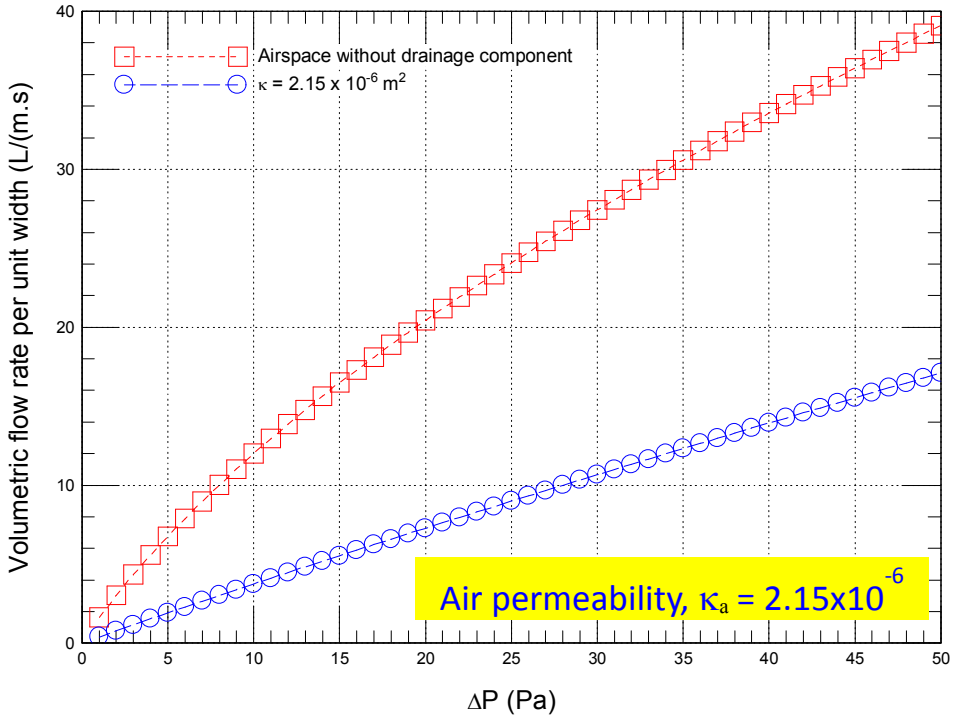


**Figure 22 – Comparison of airflow rate for cavity of 10.5 mm depth with and without drainage medium (Figure 21) of average air permeability in Y-direction**

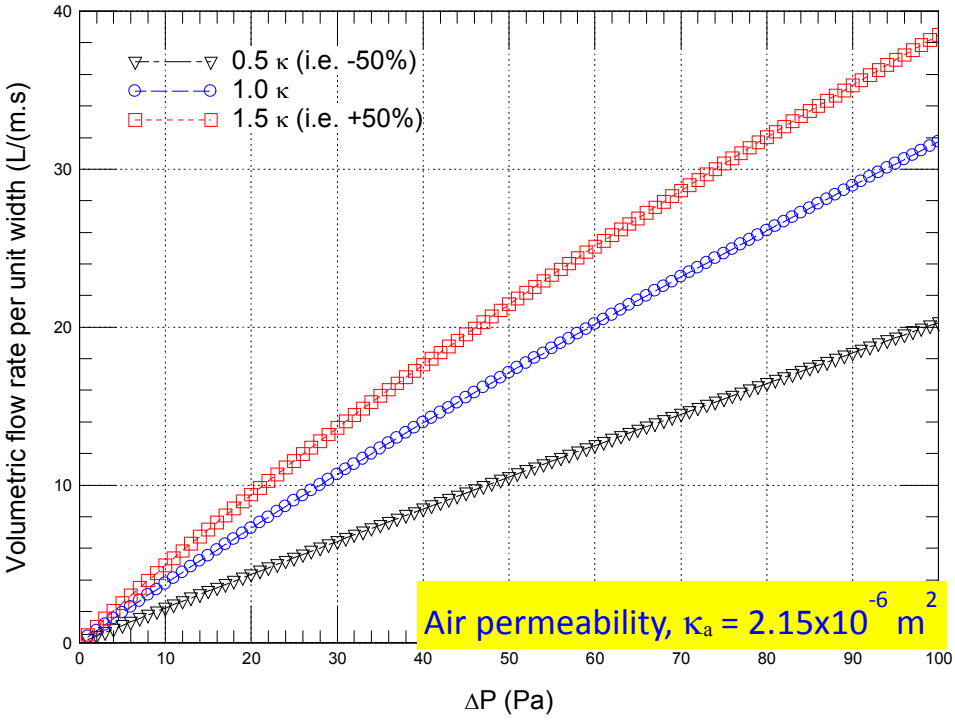


**Figure 23 – Sensitivity of volumetric air flow rate to value of air permeability ($\kappa_a$) at average $\kappa_a$ in Y-direction ± 50% for cavity of 10.5 mm depth incorporating drainage medium (Figure 21)**

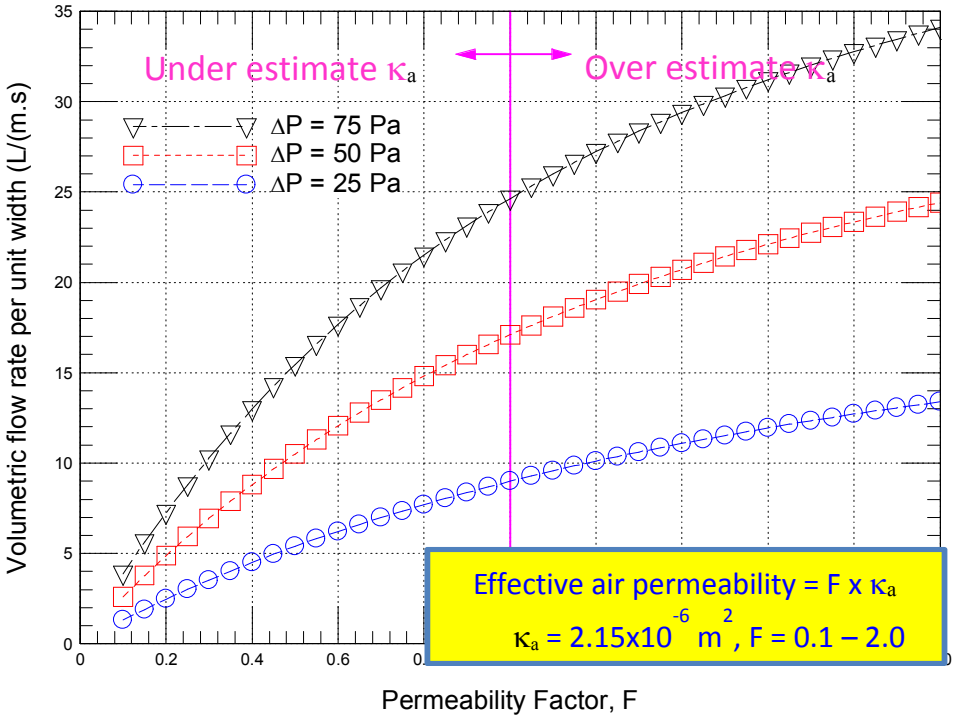


**Figure 24 – Dependence of air flow rate on dynamic permeability factor (F) and pressure differential (ΔP) at average $\kappa_a$ in Y-direction for cavity of 10.5 mm depth incorporating drainage medium (Figure 21)**

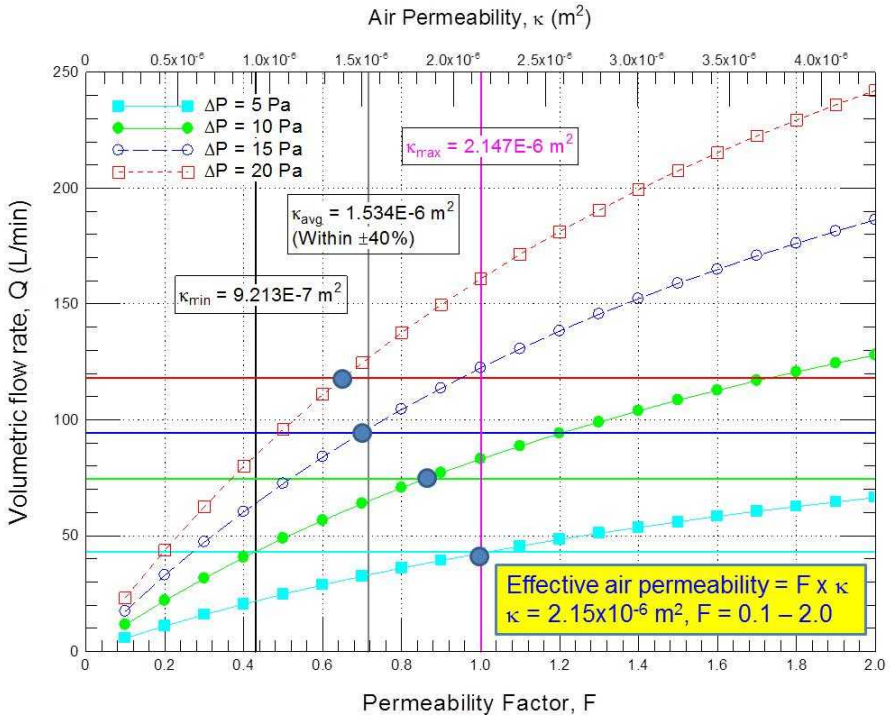


**Figure 25 – Dependence of air flow rate on dynamic permeability factor (F) at selected pressure differentials (ΔP) for cavity of 10.5 mm depth incorporating drainage medium (Figure 21)**

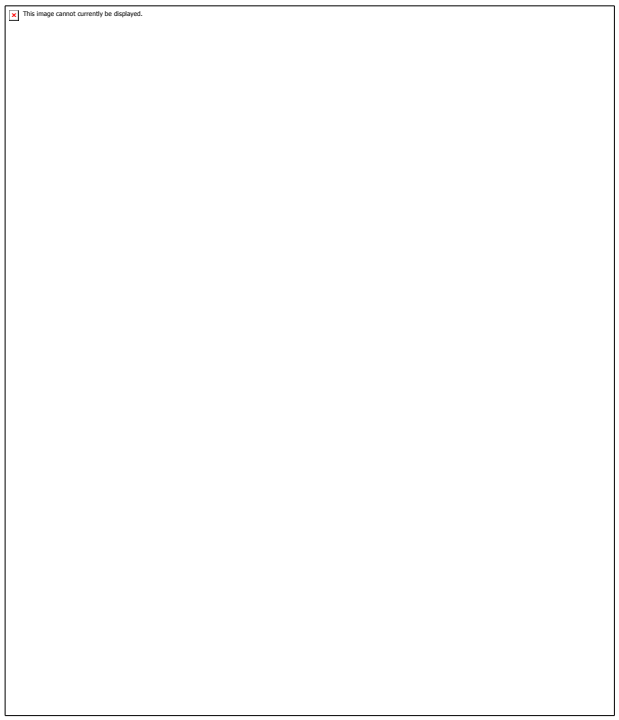

| | κ ($m^2$) | Dev (%) |
|---|---|---|
| Average of Y-Dir ($\kappa_{max}$) | 2.147E-06 | 40 |
| Average of X-Dir ($\kappa_{min}$) | 9.213E-07 | -40 |
| Avg of X- and Y-Dir ($\kappa_{avg}$) | 1.534E-06 | |

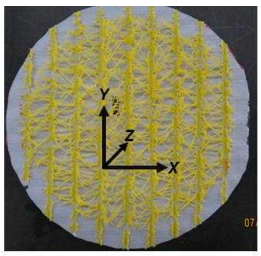


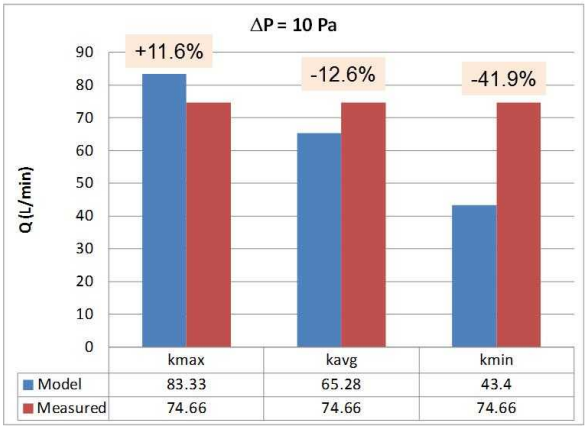


**Figure 26 – Comparison between measured volumetric air flow rate (Q) and predicted Q at ΔP = 5 Pa and at 10 Pa; value of different air permeability provided in table**

| | κ ($m^2$) | Dev (%) |
|---|---|---|
| Average of Y-Dir ($\kappa_{max}$) | 2.147E-06 | 40 |
| Average of X-Dir ($\kappa_{min}$) | 9.213E-07 | -40 |
| Avg of X- and Y-Dir ($\kappa_{avg}$) | 1.534E-06 | |

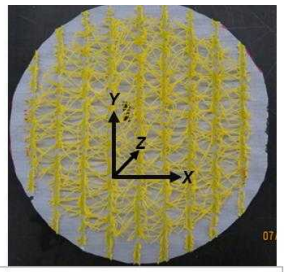


| | κ ($m^2$) | Dev (%) |
|---|---|---|
| Average of Y-Dir ($\kappa_{max}$) | 2.147E-06 | 40 |
| Average of X-Dir ($\kappa_{min}$) | 9.213E-07 | -40 |
| Avg of X- and Y-Dir ($\kappa_{avg}$) | 1.534E-06 | |

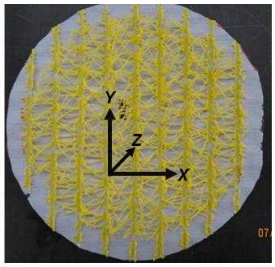


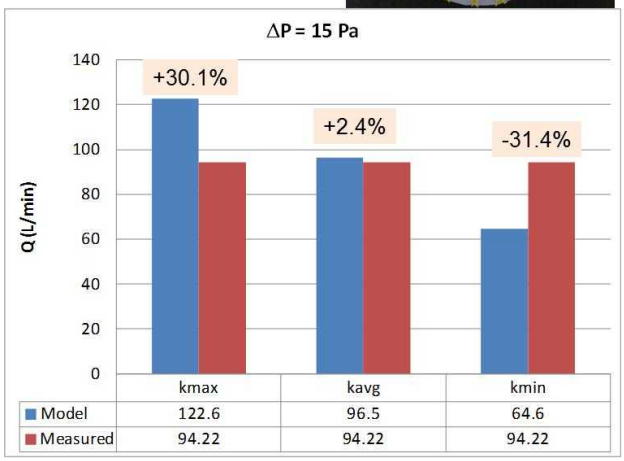


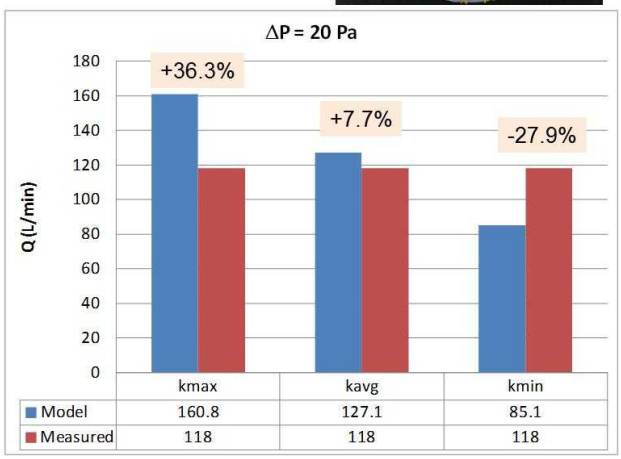


**Figure 27 – Comparison between measured volumetric air flow rate (Q) and predicted Q at ΔP = 15 Pa and at 20 Pa; value of different air permeability provided in table**

### 2.2.4 Characterization of air permeability coefficient of drainage components

To help establish the concept of how the air permeability of a highly porous media may vary due to pressure differences that arise due to the formation of eddies and vortices in the media, an example is provided of how air flow in porous media may be characterized as being laminar or turbulent and how this affects the value of air permeability for the media.

In Figure 28 is shown a porous media product (Porous polystyrene insulation board (52 mm)) of Client H and the corresponding volumetric flow rate through the media per unit area of board ($m^3 \cdot s^{-1} \cdot m^{-2}$) in relation to the pressure gradient across the board, given in $Pa \cdot m^{-1}$ (i.e. $\Delta P/L$). The characteristic curve for this relation can be given as:

$$\frac{Q}{A} = u_a = (c\nabla P)^n \qquad \text{Eq. (7)}$$

The relation, in this instance (Figure 28), plots to a straight line; as such, the flow exponent, n, is equal to 1.0. This in turn denotes that the flow in this porous media and under these pressure conditions is laminar. Additionally in the same figure, a plot is given of the effective permeability ($\kappa_a$) as a function of the volumetric flow rate and as well, a third plot of the effective permeability ($\kappa_a$) as a function of the pressure gradient across the board. The respective characteristic curves for the effective permeability are:

$$\kappa_a = a(\nabla P)^b \qquad \text{Eq. (8)}$$

$$\kappa_a = a \cdot u_a^b \qquad \text{Eq. (9)}$$

In both of these latter two plots the value of $\kappa_a$ is constant and has a value of ca. $6.3 \times 10^{-9}$ $m^2$. Of importance is the fact that for laminar flow through porous media, the permeability is constant for different pressure gradients. The flow in this porous media can be given by Eq. (1) or by Eq. (7) where the air permeability, $\kappa_a$, is constant and the flow exponent, n, equals 1.0.

Consider now the case of a different type of porous media as shown in Figure 29 (i.e. Corrugated asphalt impregnated paper board), and for which the flow through the media is characterized in the same manner as that for the porous bead board previously discussed. The data plotted in these figures are those obtained from air flow tests at different pressure gradients previously described in §2.2.1. The volumetric flow rate through the media per unit area of board ($m^3 \cdot s^{-1} \cdot m^{-2}$) in relation to the pressure gradient across the board, given in $Pa \cdot m^{-1}$ (i.e. $\Delta P/L$), is not linear but deviates from linearity, and the flow exponent, n, < 1.0; this in turn indicates that the flow in this porous media and under these pressure conditions is turbulent. The degree of deviation from linearity being a measure of the extent to which the flow in the media is turbulent as opposed to laminar.

The characteristic curve for flow through high porous media is given, as before, by Eq (7). The values for $\kappa_a$ are no longer constant but vary in accordance with either the volumetric flow rate or the pressure gradient, for which greater values of permeability are obtained at lower pressure gradients or air velocities. Thus values of permeability may range from a low of ca. $4.2 \times 10^{-7}$ $m^2$ at a pressure gradient of 20 $Pa \cdot m^{-1}$ upwards of ca. $5.5 \times 10^{-7}$ $m^2$ at the lowest pressure gradient.

Coefficients for each of the characteristic curves (Eq. (7); Eq., (8); Eq. (9)) as derived from the fitted data are provided in Figure 29. In the same manner, the air permeability characteristics of the remaining highly porous media of interest to this project were determined and this information is provided in Appendix 3 and in which the values of $\kappa_a$ for the respective drainage components used in the numerical simulation model are likewise given.

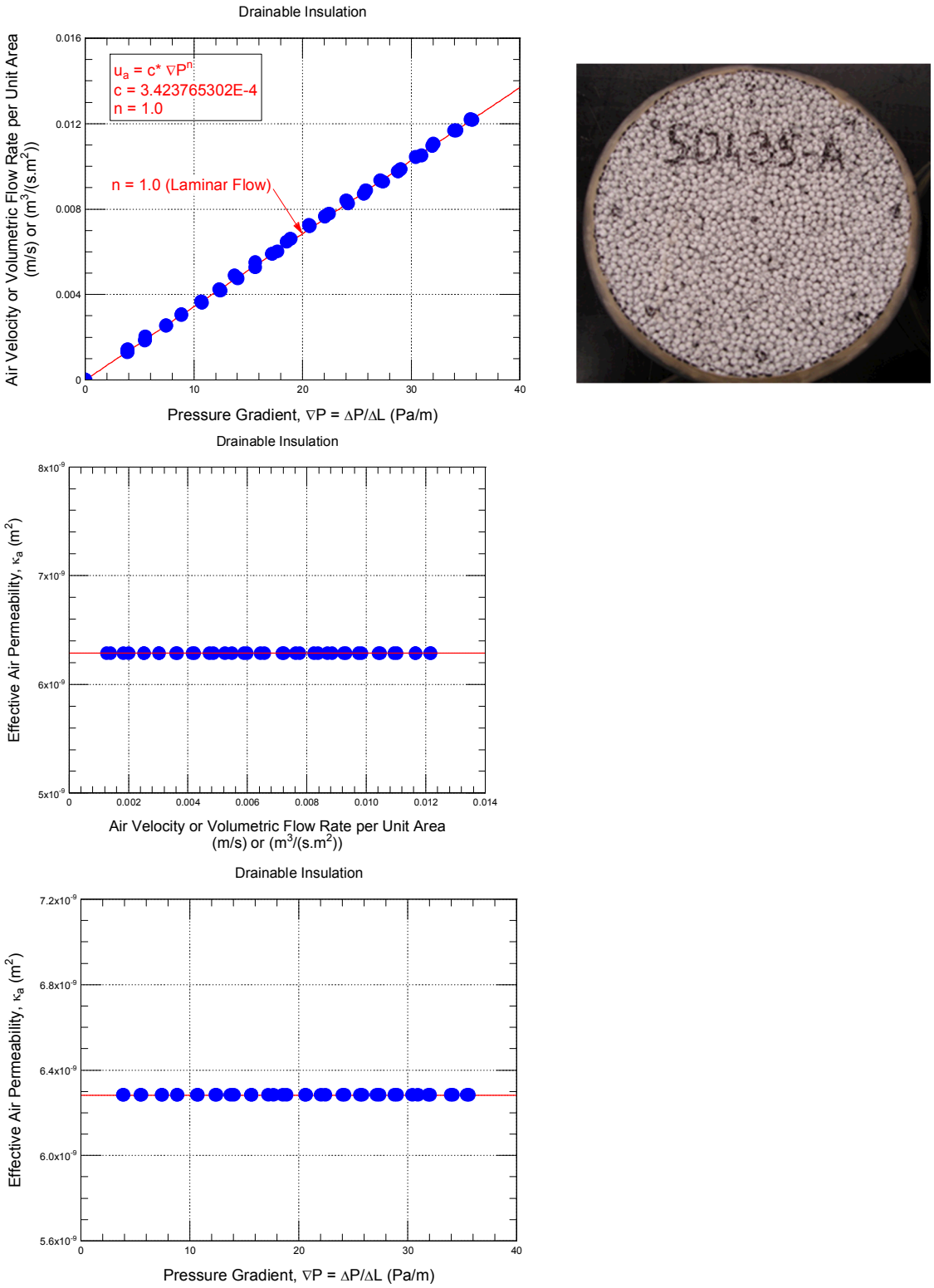


**Figure 28 – Characterization of air permeability of selected porous media (Porous polystyrene insulation board; Client H); (1) Air velocity as a function of pressure gradient; (2) Effective permeability as a function of Air velocity; (3) Effective permeability as a function of pressure gradient**

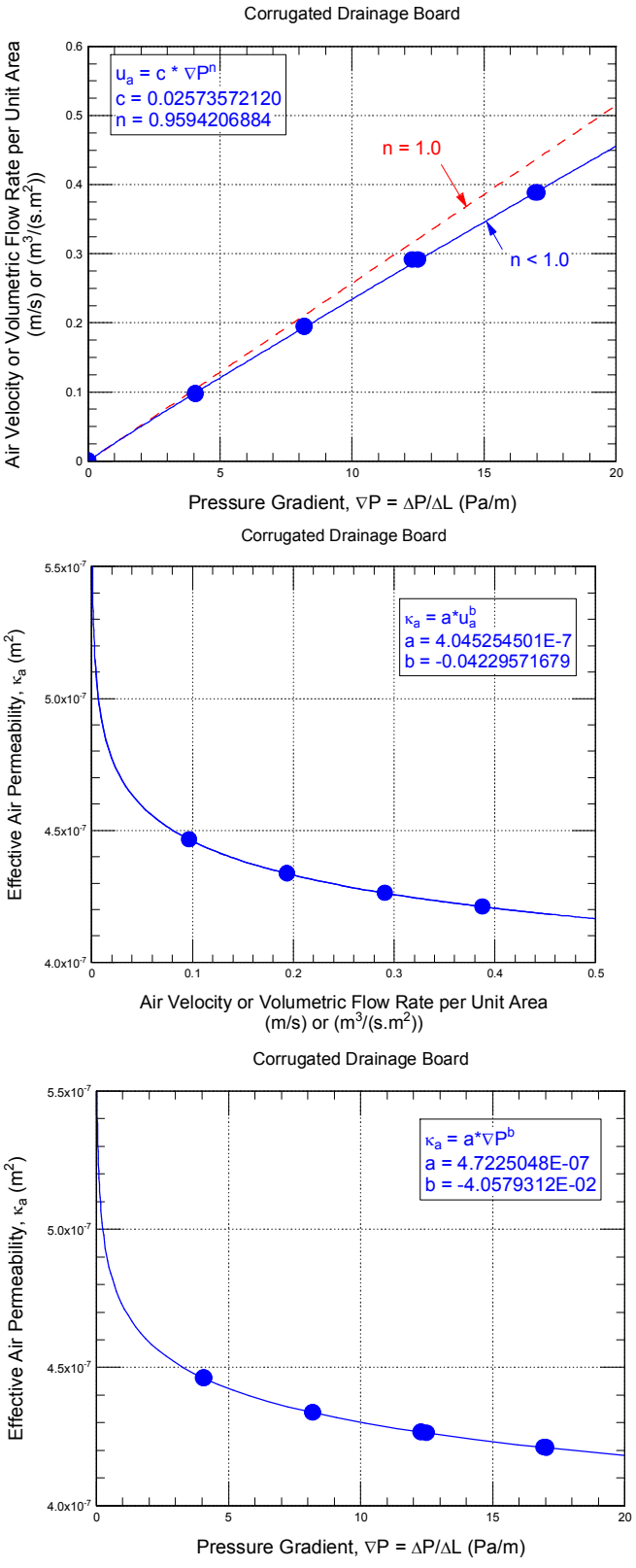


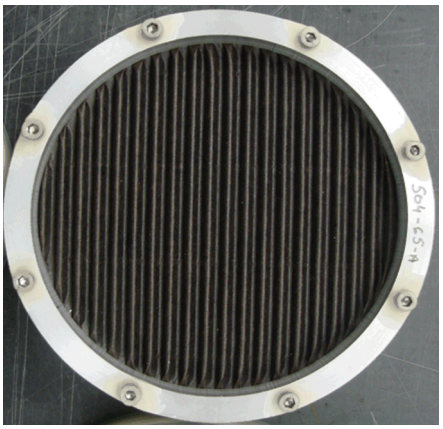

$$Q / A = u_a = c\,(\nabla P)^n \qquad \text{Eq. (7)}$$

$$\kappa_a = a\,(\nabla P)^b \qquad \text{Eq. (8)}$$

$$\kappa_a = a\,u_a^b \qquad \text{Eq. (9)}$$

| Coefficients of Eq. (7), (8) and (9) | | |
|---|---|---|
| Eq. (7) | **c** | **n** |
| | 0.0257 | 0.959 |
| Eq. (8) | $a = \mu_a \times c$ | b = n - 1 |
| | 4.72E-07 | -0.0406 |
| Eq. (9) | $a = \mu_a \times c^{(1/n)}$ | b = 1 - (1/n) |
| | 4.05E-07 | -0.0423 |

**Figure 29 – Characterization of air permeability of porous media (Corrugated asphalt impregnated paper board; Client I); (1) air velocity as a function of pressure gradient; (2) Effective permeability as a function of air velocity; (3) effective permeability as a function of pressure gradient**

## 2.3 Model Benchmarking Against Stucco Cladding Drying Test Data

This section provides the results of model benchmarking against experimental data obtained from testing to determine the rate of moisture dissipation from saturated stucco cladding when drying in laboratory conditions, the stucco mixture comprised of NBC-compliant three-coat stucco[2].

The premise of the test was to determine the rate of moisture dissipation from a stucco plate for which the drying process would be in one dimension and through only one face of the stucco plate. To help ensure that the drying test was one dimensional, the edges of the stucco plate were sealed with wax prior to soaking in a water basin. The test protocol consisted of submerging the stucco plate in water until it was saturated, and then mounting it in NRC-Construction's Wall-weighing system where its weight was recorded to a data acquisition system for the duration of the drying test; an impermeable membrane was affixed to the back side of the plate thereby helping ensure unidirectional drying. The wall-weighing system, stucco plate showing sealed edges, and the submerged stucco specimen are shown in Figure 30. The temperature and relative humidity adjacent to the surface of the stucco plate were also monitored during the test.


**Figure 30 - Wall Weighing System, Stucco Plate and Plate Wetting in Basin**

[2] NBC - National Building Code Canada 2010

The results from the drying test are given in Figure 31 for which the weight of the plate (g) is given in relation to the test duration in hours (~ 580 hrs). The red points on the plot are instances where the plate was removed from the wall-weighting system and its weight recorded independently on another weigh scale, the weight being shown on the plot. The overall weight change of the plate over the course of the tests was ca. 670 g. Measurements of temperature (T) for four locations and relative humidity in three locations are also provided on the plot; the T and RH measurements were all taken in close proximity to the plate, specifically affront the plate at its upper ("top") and lower ("bottom") periphery and behind the plate ("back"). The temperature in the laboratory ranged between ca. 18 and 25°C and the relative humidity between ca. 10 and 45% RH.

In Figure 32 is shown a graphic depicting the spatial distribution of the moisture content (in $kg_w/kg_{dm}$ %) of the stucco plate as determined from simulation at end of the test (t = 581 hrs). The direction of the moisture dissipation process is shown as is the face of the plate exposed to laboratory conditions. The results shown in the graphic suggest that most of the moisture has dissipated from the back of the plate and as well, towards the front of the plate where moisture dissipation occurred, moisture has reached equilibrium with laboratory conditions (3.6 % MC).

In Figure 33 a comparison is given between the average moisture content ($kg_w/m^3$) in the stucco plate predicted by the model and that measured by experiment in relation to the test duration in hours, whereas in Figure 34, the same comparison is shown, but provided for the moisture content in $kg_w/kg_{dm}$ of the plate. In both these figures, the variation in values of ± 5% from that predicted by the simulation model are shown with dashed lines. That the model predicts the weight of the stucco plate over the course of the test within this boundary suggests that the model is in reasonably good agreement with experimental results and that the modeling assumptions were likewise correct. As such, the model was deemed adequate to permit simulation of the moisture dissipation process for a stucco cladding conforming to the NBC.

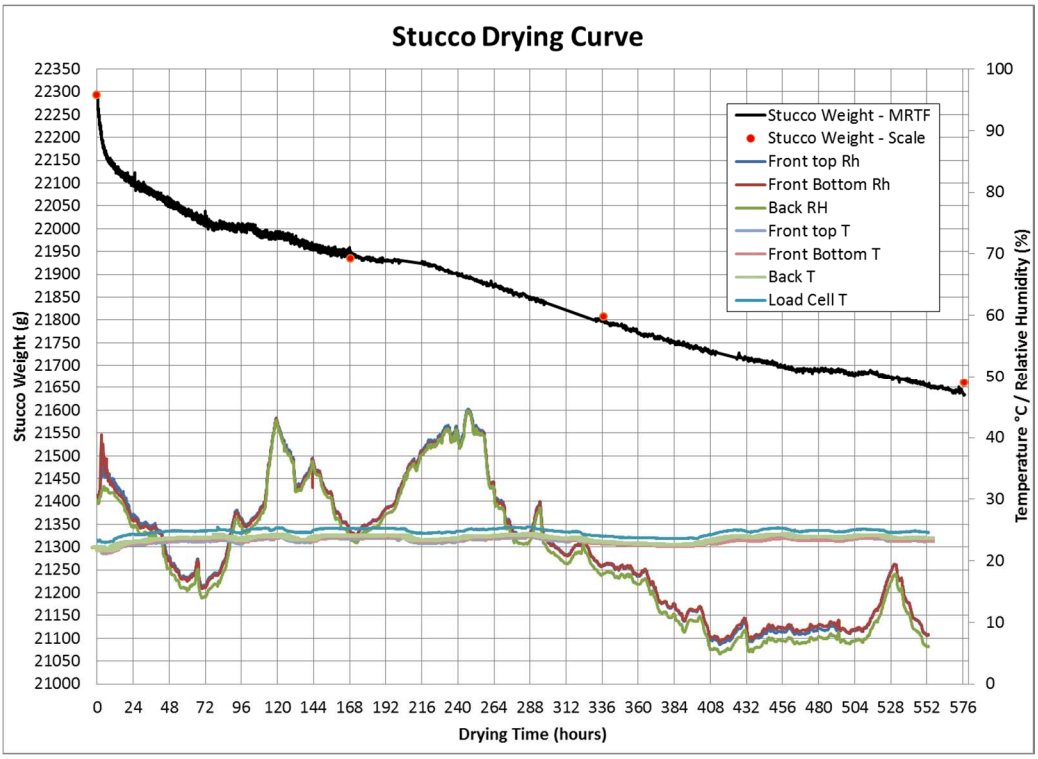


**Figure 31: Stucco Drying Rate Results by weight**

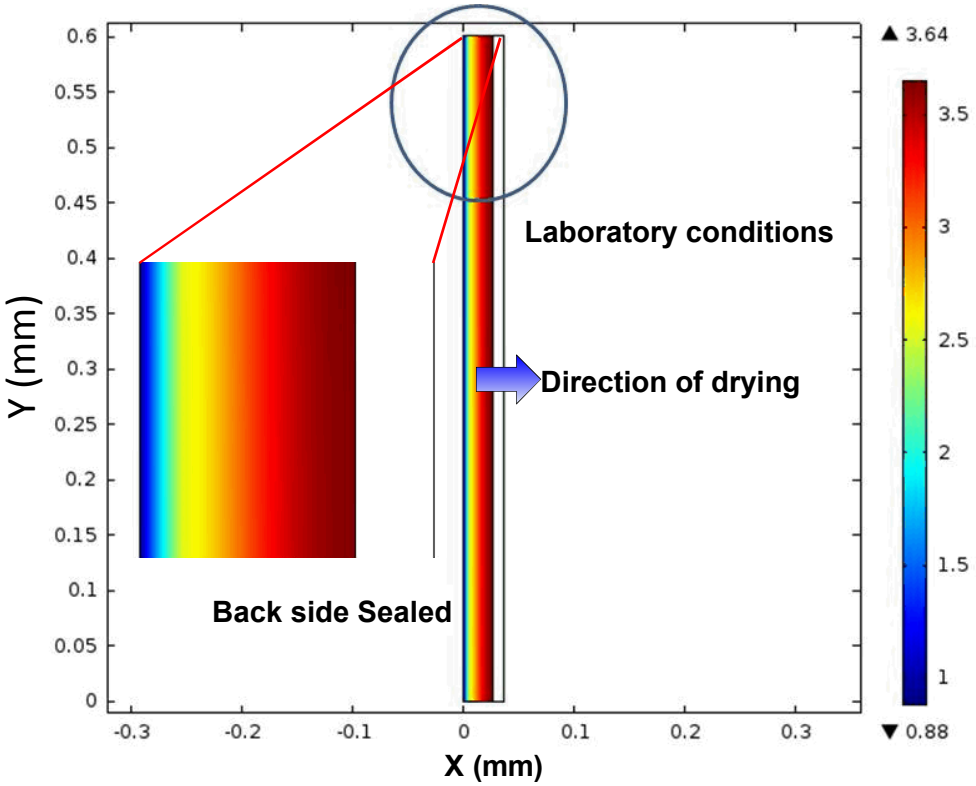


**Figure 32 – Moisture Content (MC) in $kg_w/kg_{dm}$ % at end of simulation (t = 581 hr)**

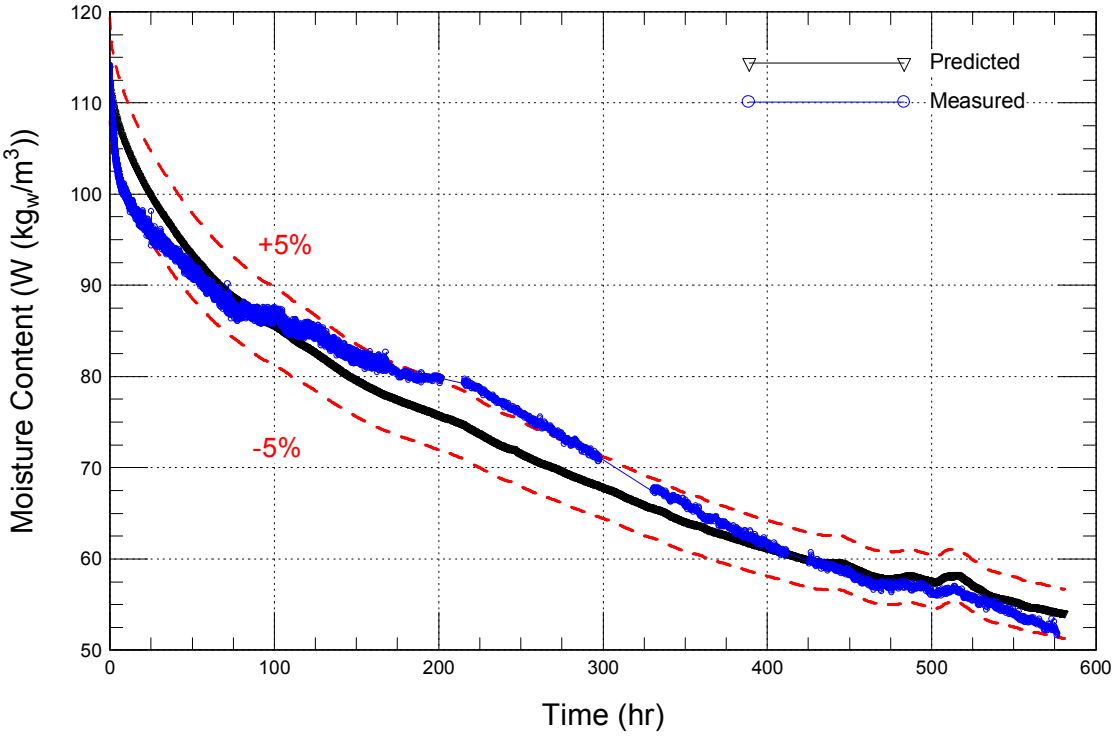


**Figure 33 – Comparison between predicted and measured average moisture content in stucco layer in $kg_w/m^3$**

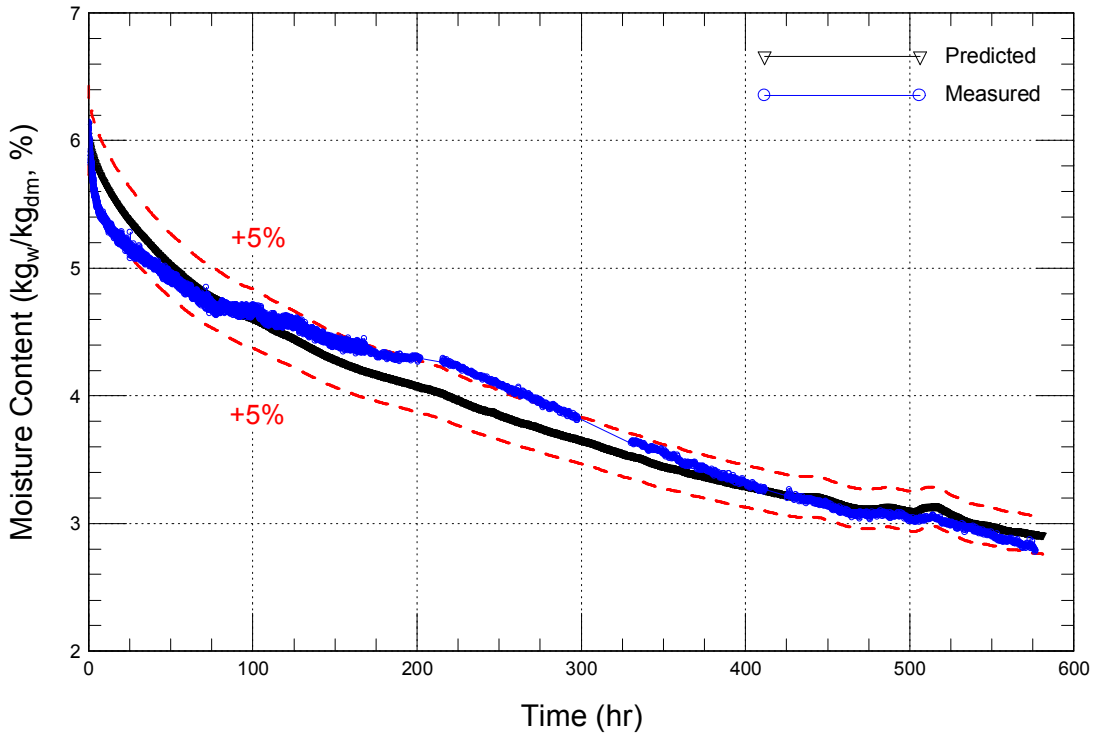


**Figure 34 – Comparison between predicted and measured average moisture content in stucco layer in $kg_w/kg_{dm}$**

# 3.0 Concluding Remarks

Task 3 of the project, as described in this report, concerns the benchmarking exercise, in which the physics of phenomena being modelled and modeling assumptions are verified prior to undertaking hygrothermal simulations of wall assemblies by comparing results of selected experimental tests to that obtained from the model; the modelling assumptions would not be deemed adequate should significant deviations from the experimental results be evident.

A description of the model and previous work undertaken to benchmark the model, are first provided and thereafter the hygrothermal model was benchmarked against the response of three different sets of experimental data to imposed laboratory test conditions, such conditions chosen to permit adequately characterizing the components in respect to a specific physical phenomenon.

These components were:

- Cavity air space behind cladding;
- Non-homogenous highly porous media (drainage components), and;
- Porous media (stucco plate).

***Cavity air space*** — The cavity air space was characterised to permit estimating from results derived from simulation for the air velocity and rate of air flow in the cavity as a function of pressure difference between inlet and outlet to cavity. The rate of flow that occurs for a given cavity depth and pressure difference across an inlet and outlet would determine the amount of moisture that could be drawn from the cavity and thus help establish the moisture balance in the cavity and from this, the presence of moisture in components of the wall assembly.

A comparison of test results to those derived from simulation showed that the majority of air velocity measurements were within the margin of uncertainty associated with the results derived from simulation for air velocity profiles obtained of cavities having depths of 10, 20 and 25 mm. Accordingly, the simulation model was used to estimate the volumetric flow rate of the cavity as a function of pressure differential across openings to the air space for different cavity depths.

***Non-homogenous highly porous media (drainage components***) — The non-homogenous highly porous media (drainage components) placed in a cavity air space were characterised to permit resolving, from simulation, the air flow in the cavity as a function of pressure difference. Given the many different types of drainage components of interest to this project, it was necessary to determine whether the presence of a drainage component significantly hindered or aided the flow of air in this air space.

An investigation was conducted to determine the air flow rates generated in the air cavity incorporating, or not, a drainage component and the sensitivity of the air flow rates to variations in air permeability coefficient ($\kappa_a$) and pressure difference. A comparison was made between the measured volumetric air flow rate (Q) and that predicted by simulation at different pressure differences. It was shown that the deviations from experiment could be minimized provided the assumed value for $\kappa_a$ is selected in relation to the pressure difference acting along the length of the cavity incorporating the drainage media. Values for the effective permeability coefficient, $\kappa_{eff}$ and corresponding values for the permeability factor, F, were

provided in relation to the pressure difference across the drainage components; these values were used in the simulation.

***Porous media (stucco plate)*** — For the porous media (stucco plate), of interest was the moisture dissipation from a stucco plate as a function of time drying in laboratory conditions. The laboratory test consisted of submerging a stucco plate in water until saturation, and thereafter monitoring the moisture dissipation over time by measuring weight changes of the plate as well as the temperature and humidity in proximity to the plate. The plate was prepared to ensure unidirectional drying by applying an impermeably membrane to the back side of the plate and by sealing the edges of the plate with wax. On this basis, the rate of moisture dissipation from the stucco plate could be determined and plotted against the results derived from simulation.

The model predicted the weight of the stucco plate over the course of the test within ± 5% of actual, suggesting that the model is in reasonably good agreement with experimental results and that the modeling assumptions were likewise correct. As such, the model was deemed adequate to permit simulation of the moisture dissipation process for a stucco cladding conforming to the NBC.

***Conclusions*** — Having previously benchmarked the hygIRC-C model to several tests undertaken in field and controlled laboratory conditions, as described above, as well as benchmarking the model against experimental data related to airflow in a cavity space incorporating, or not, drainage components, and experimental results from the drying of a stucco plate, as provided in the preceding sections, this model was used with confidence in this project to predict the hygrothermal performance of different wall assemblies having different drainage components when these walls were subjected to climatic conditions as can be found across Canada.

# 4.0 References


1. Maref, W., Saber, H.H., Glazer, R., Armstrong, M.M., Nicholls, M., Elmahdy, H., Swinton, M.C., "Energy performance of highly insulated wood-frame wall systems using a VIP", 10th International Vacuum Insulation Symposium (Ottawa, Ontario 2011-09-15), pp. 68-76.
2. Maref, W., Saber, H.H., Armstrong, M.M., Glazer, R., Ganapathy, G., Nicholls, M., Elmahdy, H., Swinton, M.C., Integration of Vacuum Insulation Panels into Canadian Wood Frame Walls, Report 1-Performance Assessment in the Laboratory, Client Report – B1253, Building Envelope Engineering Materials Program, Construction Portfolio, National Research Council of Canada, Ottawa, Canada, 2012.
3. Elmahdy, H., Maref, M., Saber, H.H., Swinton, M.C, and Glazer, R. "Assessment of the Energy Rating of Insulated Wall Assemblies a Step Towards Building Energy Labelling", 10th International Conference for Enhanced Building Operations (ICEBO2010), Kuwait, October 2010.
4. Elmahdy, A.H., Maref, W., Swinton, M.C., Saber, H.H., and Glazer, R. "Development of energy ratings for insulated wall assemblies", Building Envelope Symposium, San Diego, California, October 26, 2009, pp. 21-30.
5. Saber, H.H., Maref, W., Elmahdy, H., Swinton, M.C., and Glazer, R. "3D Heat and Air Transport Model for Predicting the Thermal Resistances of Insulated Wall Assemblies", International Journal of Building Performance Simulation, (http://dx.doi.org/10.1080/19401493.2010.532568), First published on: 24 January 2011, Vol. 5, No. 2, p. 75–91, March 2012.
6. Saber, H.H., Maref, W., Elmahdy, A.H., Swinton, M.C., and Glazer, R. "3D Thermal Model for Predicting the Thermal Resistances of Spray Polyurethane Foam Wall Assemblies", Building XI conference, Clearwater, Florida, 2010.
7. Maref, W., Saber, H.H., Ganapathy, G., and Nicholls, M., Field Energy Performance and Hygrothermal Evaluation of Different Strategies of Energy Retrofit for Residential Wood-Frame Wall Systems Field using VIP, Client report B-1266.3, National Research Council of Canada, Ottawa, August 2012.
8. Saber, H.H., Maref, W., Lacasse, M.A., Swinton, M.C., and Kumaran, K. "Benchmarking of Hygrothermal Model against Measurements of Drying of Full-Scale Wall Assemblies" International Conference on Building Envelope Systems and Technologies, ICBEST 2010, Vancouver, Canada, June 27-30, 2010.
9. Saber, H.H., Maref, W., and Swinton, M.C. "Thermal Response of Basement Wall Systems with Low Emissivity Material and Furred Airspace" *Journal of Building Physics,* vol. 35, no. 2, pp. 353-371, 2012, (NRCC-53962).
10. Saber, H.H., Maref, W., Armstrong, M.M., Swinton, M.C., Rousseau, M.Z., and Ganapathy, G., "Benchmarking 3D Thermal Model against Field Measurement on the Thermal Response of an Insulating Concrete Form (ICF) Wall in Cold Climate", Eleventh International Conference on Thermal Performance of the Exterior Envelopes of Whole Buildings XI (Clearwater, FL, USA, December 4-9, 2010).
11. Armstrong, M., Saber, H.H., Maref, W., Rousseau, M.Z., Ganapathy, G., and Swinton, M.C., "Field Energy Performance of an Insulating Concrete Form (ICF) Wall", 13th CCBST conference - Winnipeg 2011, The 13th Canadian Conference on Building Science and Technology, Winnipeg, Manitoba May 10 – 13, 2011.
12. Saber, H.H., Swinton, M.C. "Determining through Numerical Modeling the Effective Thermal Resistance of a Foundation Wall System with Low Emissivity Material and Furred – Airspace" International Conference on Building Envelope Systems and Technologies, ICBEST 2010, Vancouver, Canada, June 27-30, 2010.

13. Saber, H.H., Maref, W., Swinton, M.C., and St-Onge, C., "Thermal analysis of above-grade wall assembly with low emissivity materials and furred-airspace," Journal of Building and Environment, volume 46, issue 7, pp. 1403-1414, 2011 (doi:10.1016/j.buildenv.2011.01.009).

14. Saber, H.H, and Laouadi, A. "Convective Heat Transfer in Hemispherical Cavities with Planar Inner Surfaces (1415-RP)" Journal of ASHRAE Transactions, Volume 117, Part 2, 2011.

15. Saber, H.H., and Maref, W., "Effect of Furring Orientation on Thermal Response of Wall Systems with Low Emissivity Material and Furred-Airspace", The Building Enclosure Science & Technology (BEST3) Conference, held in April 2-4, 2012 in Atlanta, Georgia, USA.

16. Saber, H.H., "Thermal Performance of Wall Assemblies with Low Emissivity" Journal of Building Physics, DOI: 10.1177/1744259112450419, in press, May 2012.

17. Saber, H.H., "Investigation of Thermal Performance of Reflective Insulations for Different Applications" Journal of Building and Environment, 52, p. 32-44, 2012 (doi:10.1016/j.buildenv.2011.12.010).

18. Saber, H.H., Maref, W., Sherrer, G., Swinton, M.C. "Numerical Modelling and Experimental Investigations of Thermal Performance of Reflective Insulations", Journal of Building Physics, The online version of this article can be found at: http://jen.sagepub.com/content/early/2012/04/25/1744259112444021, April 2012.

19. Saber, H.H., Swinton, M.C., Kalinger, P., and Paroli, R.M., "Hygrothermal Simulations of Cool Reflective and Conventional Roofs", 2011 NRCA International Roofing Symposium, Emerging Technologies and Roof System Performance, held in Sept. 7-9, 2011, Washington D.C., USA.

20. Saber, H.H., Swinton, M.C., Kalinger, P., and Paroli, R.M., "Long-Term Hygrothermal Performance Of White And Black Roofs In North American Climates", Journal of Building and Environment, 50, p. 141-154, 2012, DOI: 10.1016/j.buildenv.2011.10.022, http://dx.doi.org/10.1016/j.buildenv.2011.10.022.

21. Armstrong, M., Maref, W., Saber, H.H., Rousseau, M.Z., Ganapathy, G., Swinton, M.C., "The impact of the thermal mass on field energy performance of insulating concrete form (ICF) wall" International Workshop on Whole Building Testing, Evaluation and Modelling for Energy Assessment (Copenhagen, Denmark 2011-05-18), pp. 1-12.

22. Saber, H.H., Maref, W., Armstrong, M.M., Swinton, M.C., Rousseau, M.Z., Ganapathy, G. "Numerical Simulations to Predict the Thermal Response of Insulating Concrete Form (ICF) Wall in Cold Climate ", Research Report-310, NRC Inst. for Research in Construction, 310, 2011-04-01.

23. Maref, W., Kumaran, M.K., Lacasse, M.A., Swinton, M.C., and van Reenen, D. "Laboratory measurements and benchmarking of an advanced hygrothermal model", Proc. 12th International Heat Transfer Conference, Grenoble, France, Aug. 18, 2002, pp. 117-122 (NRCC-43054).

24. Saber, H.H., "Practical Correlation for Thermal Resistance of Low-Sloped Enclosed Airspaces with Downward Heat Flow for Building Applications", HVAC&R Research Journal, DOI:10.1080/10789669.2013.834779, http://dx.doi.org/10.1080/10789669.2013.834779, pp. 1-33, October 2013.

25. Saber, H.H., "Practical Correlation for Thermal Resistance of Horizontal Enclosed Airspaces with Downward Heat Flow for Building Applications", Journal of Building Physics, DOI: 10.1177/1744259113498473, the online version of this article can be found at: http://jen.sagepub.com/content/early/2013/08/19/1744259113498473, in press, July 2013.

26. Saber, H.H., "Practical Correlation for Thermal Resistance of 45° Sloped Enclosed Airspaces with Downward Heat Flow for Building Applications", Journal of Building and Environment, http://dx.doi.org/10.1016/j.buildenv.2013.04.009, volume 65, pp. 154-169, 2013.

27. Saber, H.H., "Practical Correlations for Thermal Resistance of Horizontal Enclosed Airspaces with Upward Heat Flow for Building Applications", Journal of Building and Environment, http://dx.doi.org/10.1016/j.buildenv.2012.12.016, vol. 61, pp. 169-187, 2013.

28. Saber, H.H., "Practical Correlations for the Thermal Resistance of Vertical Enclosed Airspaces for Building Applications", Journal of Building and Environment, http://dx.doi.org/10.1016/j.buildenv.2012.09.003, vol. 59, pp. 379-396, January 2013.

29. Saber, H.H., Maref, W., Gnanamurugan, G., and Nicholls, M., "Energy Retrofit Using VIPs - an Alternative Solution for Enhancing the Thermal Performance of Wood-Frame Walls", Journal of Building Physics, DOI: 10.1177/1744259113505748, the online version of this article can be found at: http://jen.sagepub.com/content/early/2013/10/15/1744259113505748, pp. 1-34, October 2013.

30. Saber, H.H., Maref, W., Gnanamurugan, G. and Nicholls, M. "Model Benchmarking for Field Energy Retrofit towards Highly Insulated Residential Wood-Frame Construction Using VIPs" 11th International Vacuum Insulation Symposium (IVIS2013), September 19-20, 2013, EMPA, Switzerland.

31. Maref, W., Saber, H.H., Gnanamurugan, G. and Nicholls, M. "In-Situ Performance of Residential Wood-Frame Construction Retrofitted Using VIPs" 11th International Vacuum Insulation Symposium (IVIS2013), September 19-20, 2013, EMPA, Switzerland.

32. ASTM C 1363, Standard Test Method for the Thermal Performance of Building Assemblies by Means of a Hot Box Apparatus, 2006 Annual Book of ASTM Standards 04.06:717–59, www.astm.org.

33. ASTM C 518-04, Steady-State Thermal Transmission Properties by Means of the Heat Flow Meter Apparatus, Section 4, Volume 04.06, Thermal Insulation, 2007 Book of ASTM Standards.

34. ASHRAE. 2009. ASHRAE Handbook –Fundamentals (SI), Chapter 26, Atlanta: American Society of Heating, Refrigerating, and Air-Conditioning Engineers Inc.

35. Mukhopadhyaya, P., and Van Reenen, D., Heat Flow Characterization of Three GDDC (Geometrically Defined Drainage Cavity) Specimens, Client Report: A1-003165.1, National Research Council of Canada, Construction Portfolio, Ottawa, Canada, July 2013.

36. ASTM C 177-04, Standard Test Method for Steady-State Heat Flux Measurements and Thermal Transmission Properties by Means of the Guarded-Hot-Plate Apparatus, Section 4, Volume 04.06, Thermal Insulation, 2012 Book of ASTM Standards.

37. Saber, H.H., Maref, W. and Abdulghani, K., Properties and Position of Materials in the Building Envelope for Housing and Small Buildings, Report No. A1-004615.1, NRC-Construction, National Research Council of Canada, Ottawa, Canada, December, 31, 2014.

38. Saber, H.H., "Thermal Resistance of Enclosed Reflective Airspaces in Building Applications", BEST Building Enclosure Science & Technology Conference (BEST4), to be held in April 12-15, 2015, Kansas City, Missouri, USA.

39. Kumaran, M. K., & Bomberg, M. T. (1986). "A Test Method to Determine Air Flow Resistance of Exterior Membranes and Sheathings", Journal of Thermal Insulation, 9: 224-235.

# Appendix 1 – List of Task Reports

| Report | Reference |
|---|---|
| **Task 1** | M. Armstrong and B. Di Lenardo (2014), Performance Evaluation of Proprietary Drainage Components and Sheathing Membranes when Subjected to Climate Loads – Task 1 – Wall Assembly Specifications; Client Report A1-000030.01; National Research Council Canada; Ottawa, ON; 52 pgs. |
| **Task 2** | P. Mukhopadhyaya, D. van Reenen and S. Bundalo-Perc (2014), Performance Evaluation of Proprietary Drainage Components and Sheathing Membranes when Subjected to Climate Loads – Task 2 – Building Component Hygrothermal Properties Characterization; Client Report A1-000030.02; National Research Council Canada; Ottawa, ON; 58 pgs. |
| **Task 3** | H. H. Saber, W. Maref, and G. Ganapathy, (2015) Performance Evaluation of Proprietary Drainage Components and Sheathing Membranes when Subjected to Climate Loads – Task 3 –Hygrothermal Model Benchmarking; Client Report A1-000030.04; National Research Council Canada; Ottawa, ON; 63 pgs. |
| **Task 4** | W. Maref, H. H. Saber and G. Ganapathy (2015), Performance Evaluation of Proprietary Drainage Components and Sheathing Membranes when Subjected to Climate Loads – Task 4 – Characterization of Air Flow within Drainage Cavities; Client Report A1-000030.05; National Research Council Canada; Ottawa, ON; 115 pgs. |
| **Task 5** | Steven M. Cornick and Khaled Abdulghani (2013), Performance Evaluation of Proprietary Drainage Components and Sheathing Membranes when Subjected to Climate Loads – Task – Defining Exterior Environmental Loads; Client Report A1-000030.03; National Research Council Canada; Ottawa, ON; 99 pgs. |
| **Task 5** | T. Moore and M. A. Lacasse (2015), Performance Evaluation of Proprietary Drainage Components and Sheathing Membranes when Subjected to Climate Loads – Task 5 – Characterization of Water Entry to, Retention and Dissipation from Drainage Components; Client Report A1-000030.06; National Research Council Canada; Ottawa, ON; 43 pgs. |
| **Task 6** | H. H. Saber and M. A. Lacasse (2015) Performance Evaluation of Proprietary Drainage Components and Sheathing Membranes when Subjected to Climate Loads – Task 6 – Hygrothermal Performance of NBC-Compliant Reference Walls for Selected Canadian Locations, Client Report A1-000030.07; National Research Council Canada; Ottawa, ON; 59 pgs. |
| **Task 6** | H. H. Saber et al. (2015) Performance Evaluation of Proprietary Drainage Components and Sheathing Membranes when Subjected to Climate Loads – Task 6 – Hygrothermal Performance of Wall Assemblies with Cavities or Incorporating Drainage Components for Selected Canadian Locations; Client Report A1-000030.08; National Research Council Canada; Ottawa, ON. |
| **Task 7** | M. A. Lacasse (2015) Performance Evaluation of Proprietary Drainage Components and Sheathing Membranes when Subjected to Climate Loads – Task 7 – Summary Report on Experimental and Modelling Tasks and Recommendations; Client Report A1-000030.09; National Research Council Canada; Ottawa, ON. |

## Appendix 2 – Cavity Air Velocity Measurements Compared to those Derived from Simulation

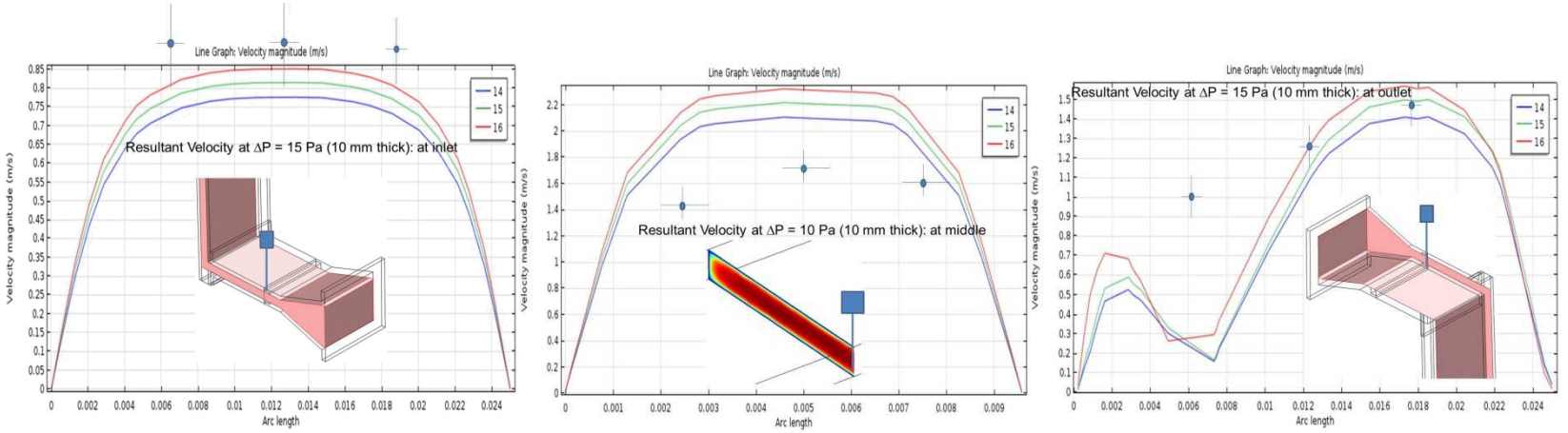


**Figure 35 – Comparison of velocity measurements for an airspace of 10 mm depth with test data at the inlet, middle and outlet of the airspace at ΔP = 15.0 Pa ± 1.0 Pa**

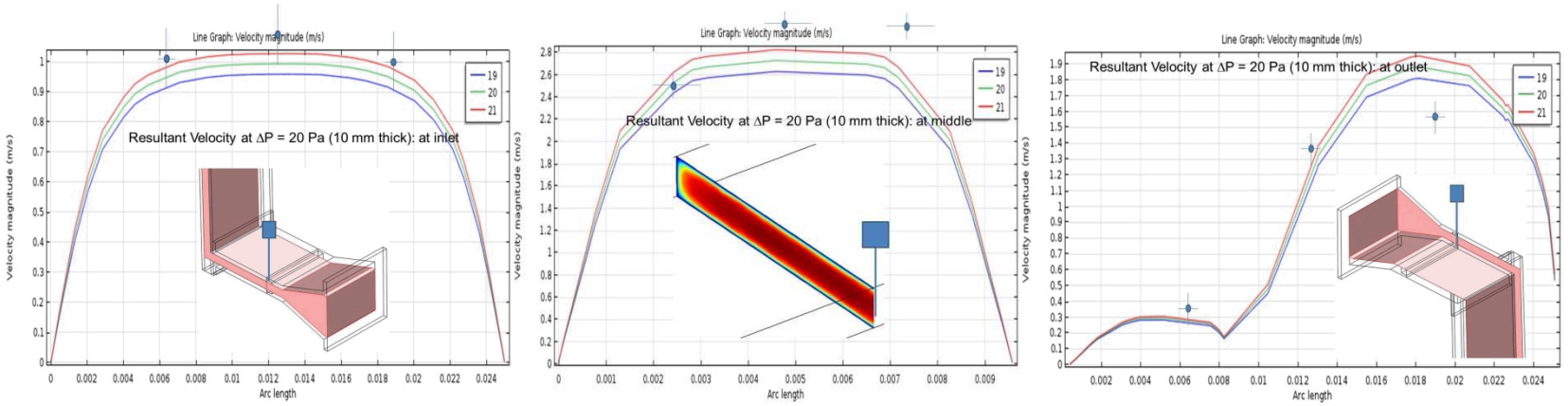


**Figure 36 – Comparison of velocity measurements for an airspace of 10 mm depth with test data at the inlet, middle and outlet of the airspace at ΔP = 20.0 Pa ± 1.0 Pa**

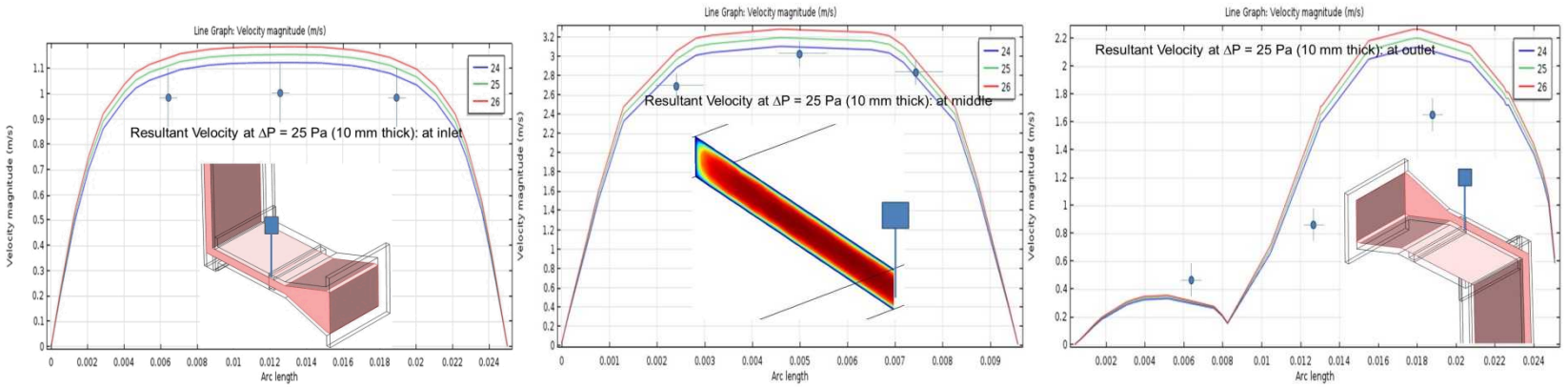


**Figure 37 – Comparison of velocity measurements for an airspace of 10 mm depth with test data at the inlet, middle and outlet of the airspace at ΔP = 25.0 Pa ± 1.0 Pa**

| Inlet location | Middle cavity location | Outlet location |
|---|---|---|

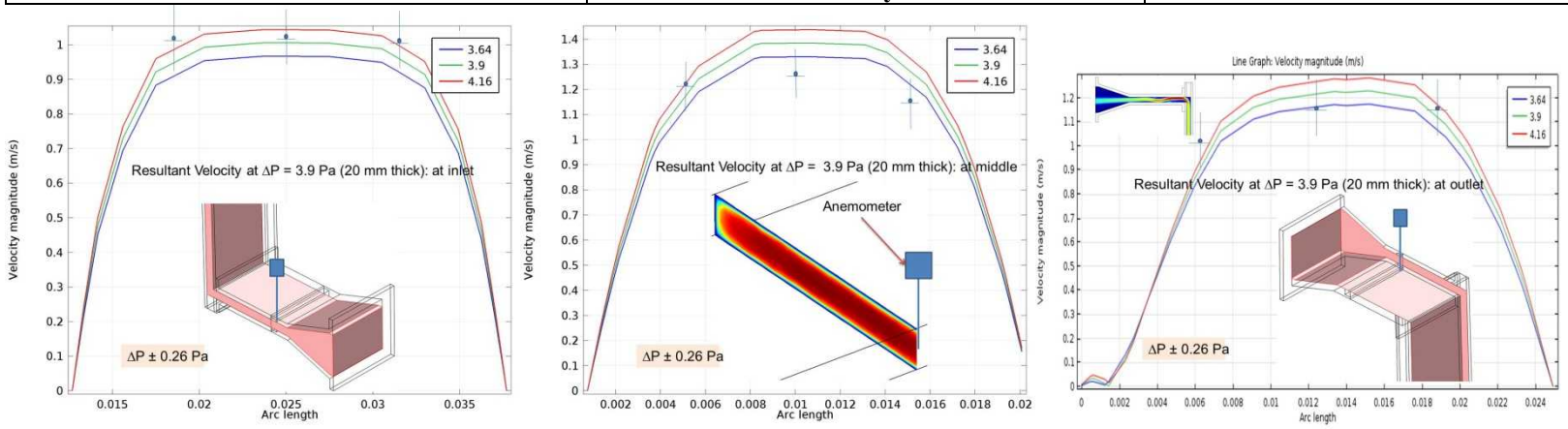


**Figure 38 – Comparison of velocity measurements for an airspace of 20 mm depth with test data at the inlet, = middle and outlet of the cavity at ΔP = 3.9 Pa ± 0.26 Pa**

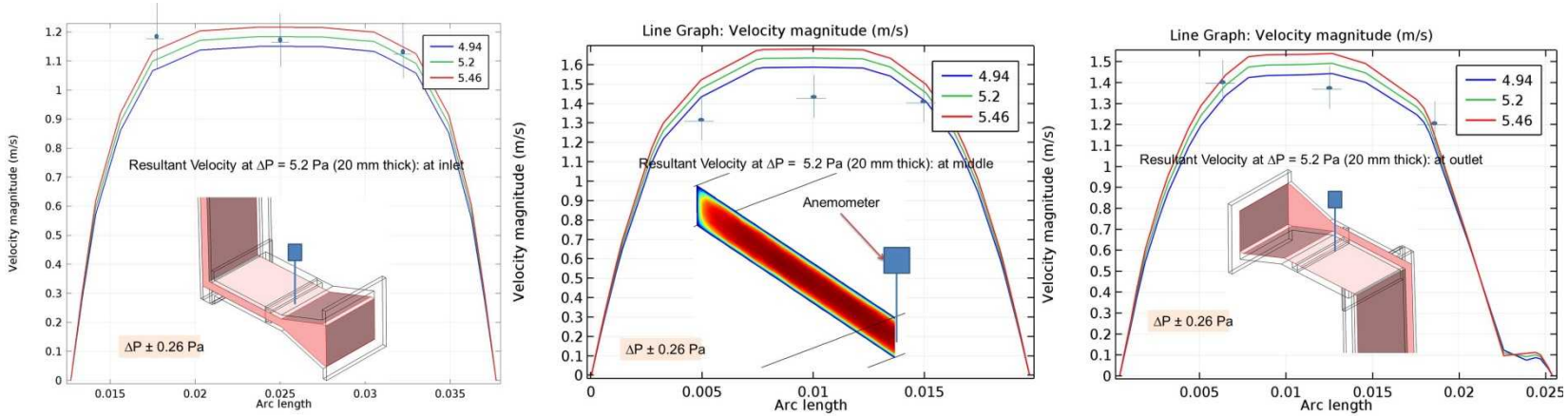


**Figure 39 – Comparison of velocity measurements for an airspace of 20 mm depth with test data at the inlet, middle and outlet of the cavity at ΔP = 5.2 Pa ± 0.26 Pa**

| Inlet location | Middle cavity location | Outlet location |
|---|---|---|

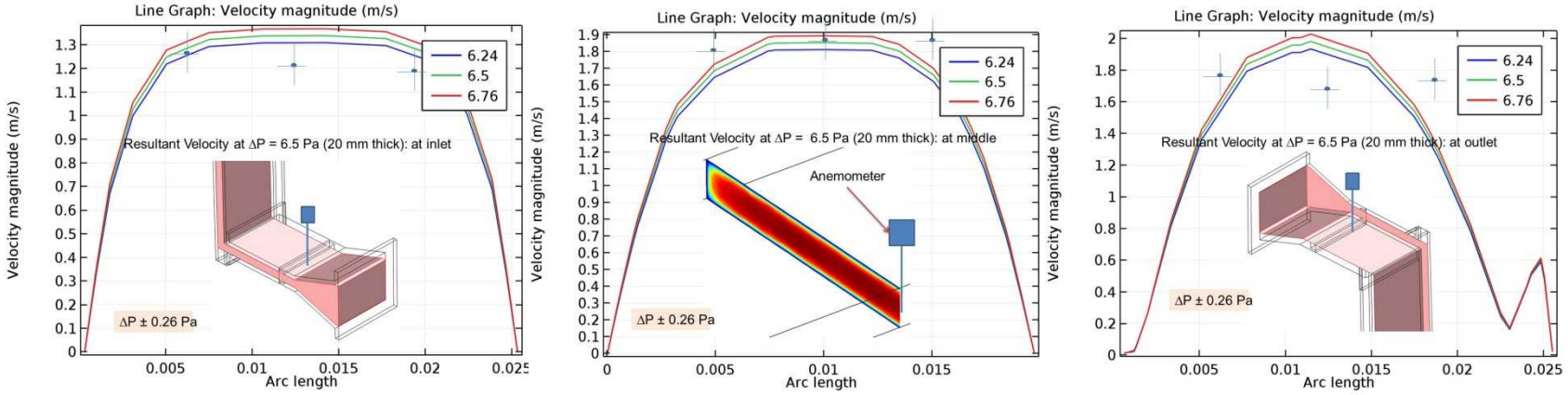


**Figure 40 – Comparison of velocity measurements for an airspace of 20 mm depth with test data at the inlet, middle and outlet of the cavity at ΔP = 6.5 Pa ± 0.26 Pa**

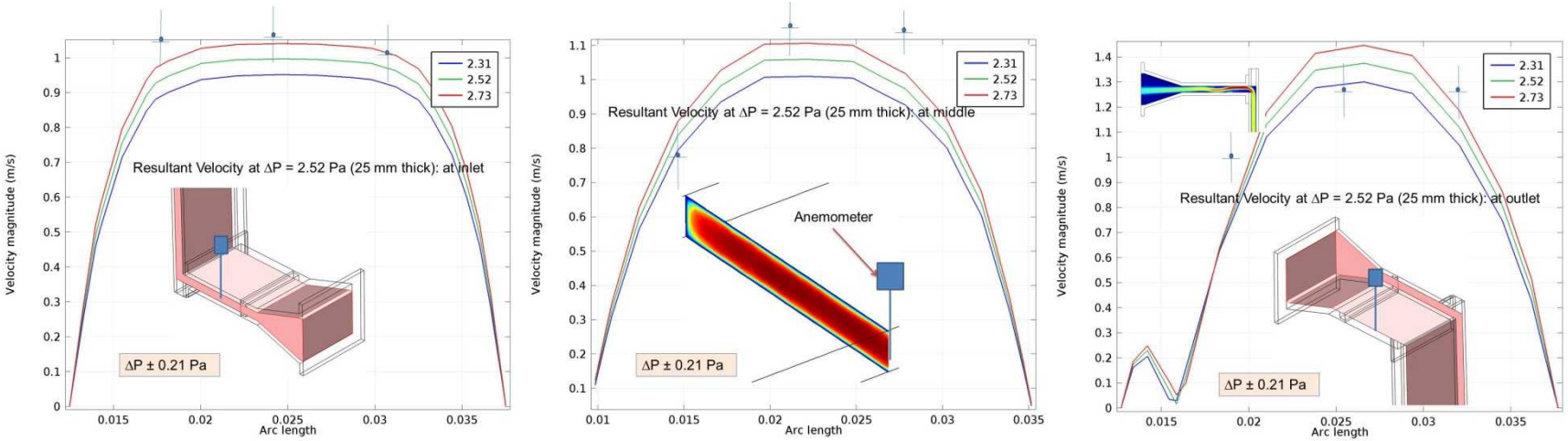


**Figure 41 – Comparison of velocity measurements for an airspace of 25 mm depth with test data at the inlet, middle and outlet of the airspace at ΔP = 2.52 Pa ± 0.21 Pa**

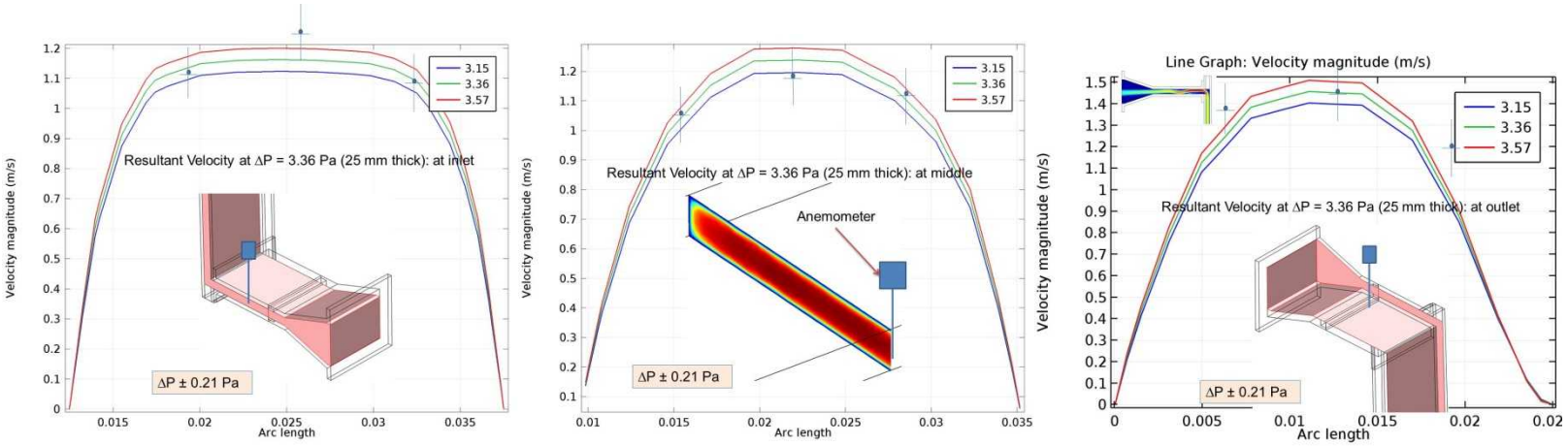


**Figure 42 – Comparison of velocity measurements for an airspace of 25 mm depth with test data at the inlet, middle and outlet of the airspace at ΔP = 3.63 Pa ± 0.21 Pa**

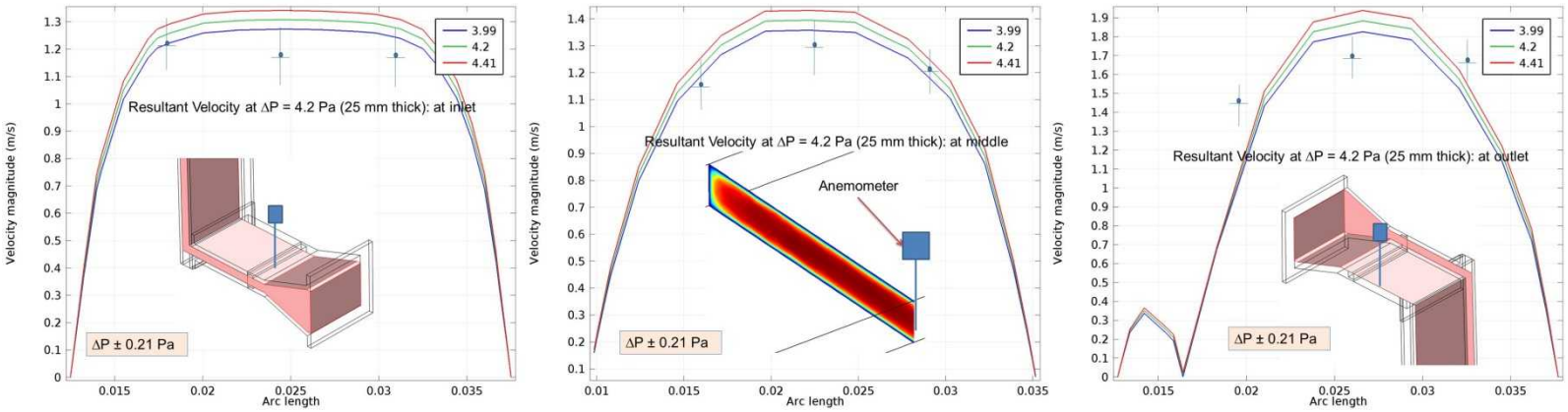


**Figure 43 – Comparison of velocity measurements for an airspace of 25 mm depth with test data at the inlet, middle and outlet of the airspace at ΔP = 4.2 Pa ± 0.21 Pa**

# Appendix 3 –Characterization of Air Permeability of Non-homogenous and Highly Permeable Drainage Components

## Dimpled HDPE[3] membrane; Client E

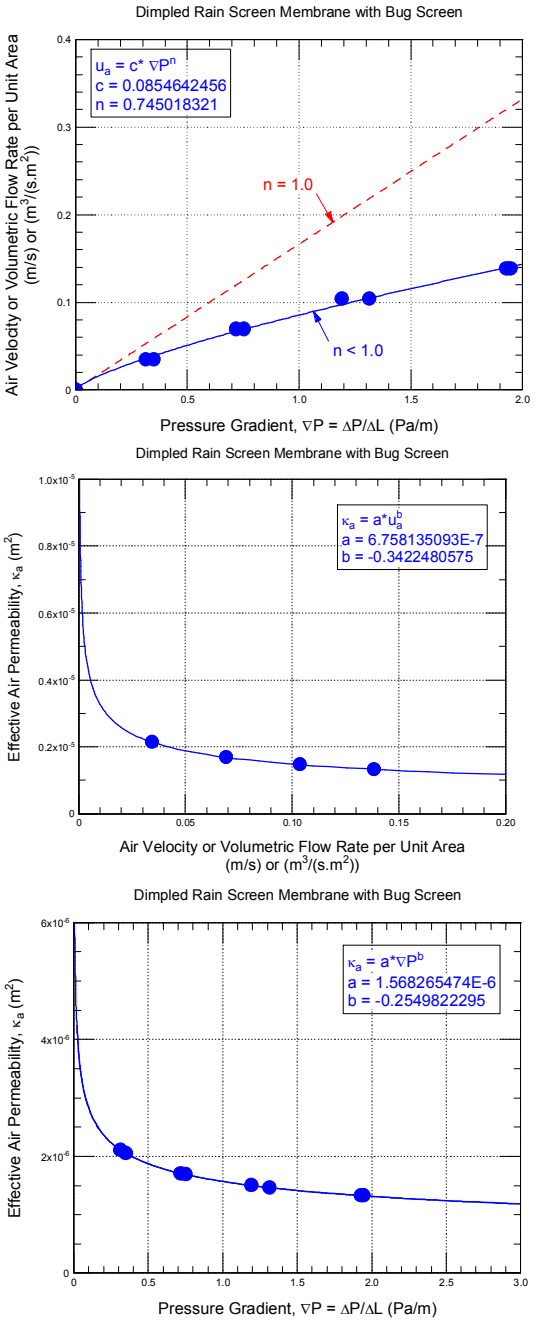


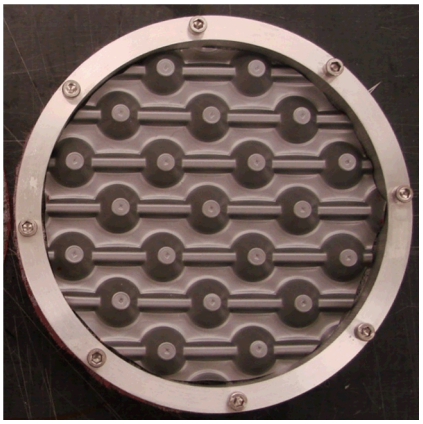

$$Q / A = u_a = c\,(\nabla P)^n \qquad \text{Eq. (7)}$$

$$\kappa_a = a\,(\nabla P)^b \qquad \text{Eq. (8)}$$

$$\kappa_a = a\,u_a^b \qquad \text{Eq. (9)}$$

| Coefficients of Eq. (7), (8) and (9) | | |
|---|---|---|
| Eq. (7) | c | n |
| | 0.0855 | 0.7450 |
| Eq. (8) | $a = \mu_a \times c$ | b = n - 1 |
| | 1.568E-06 | -0.2550 |
| Eq. (9) | $a = \mu_a \times c^{(1/n)}$ | b = 1 - (1/n) |
| | 6.758E-07 | -0.3422 |

**Figure 44 – Characterization of air permeability of porous media (Dimpled HDPE membrane Client E); (1) air velocity as a function of pressure gradient; (2) effective permeability as a function of Air velocity; (3) effective permeability as a function of pressure gradient**

[3] HDPE – high density polyethylene

## Non-woven PP[4] fabric (stucco screen) bonded to PP mono-filament mesh; Client G

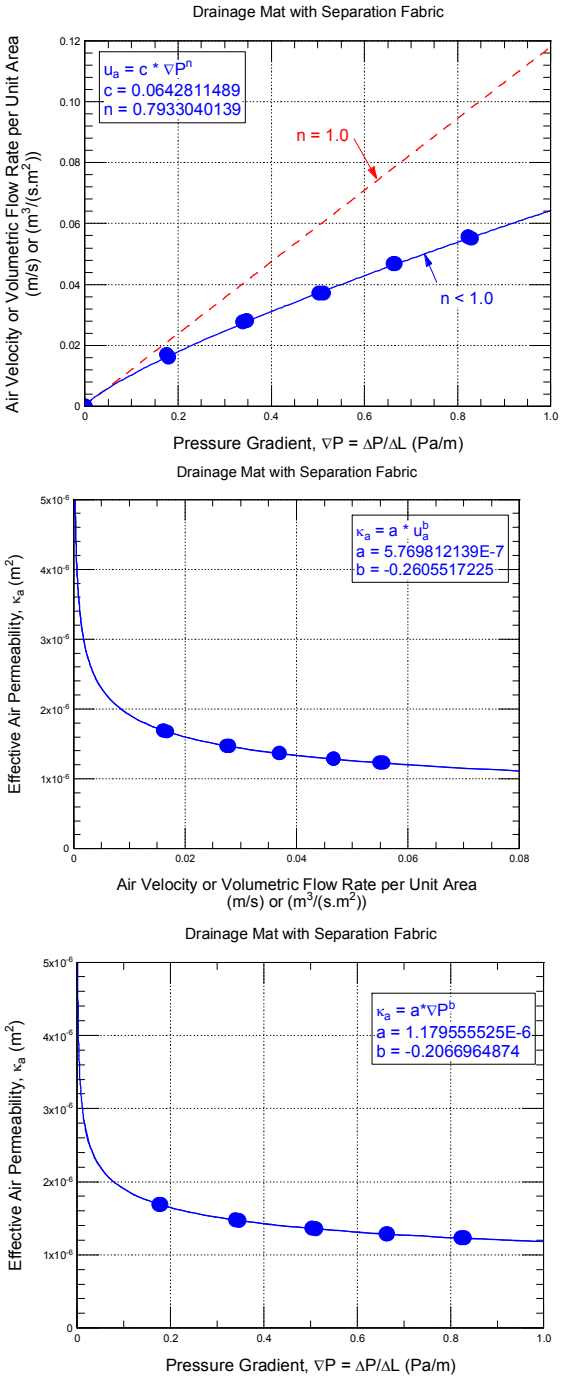


$$Q / A = u_a = c\,(\nabla P)^n \qquad \text{Eq. (7)}$$

$$\kappa_a = a\,(\nabla P)^b \qquad \text{Eq. (8)}$$

$$\kappa_a = a\,u_a^b \qquad \text{Eq. (9)}$$

| Coefficients of Eqs. (7), (8) and (9) | | |
|---|---|---|
| Eq. (7) | c | n |
| | 0.0643 | 0.7933 |
| Eq. (8) | $a = \mu_a \times c$ | b = n - 1 |
| | 1.1796E-06 | -0.2067 |
| Eq. (9) | $a = \mu_a \times c^{(1/n)}$ | b = 1 - (1/n) |
| | 5.769E-07 | -0.2606 |

**Figure 45 – Characterization of air permeability of porous media (Non-woven PP fabric bonded to PP mono-filament mesh; Client G); (1) air velocity as a function of pressure gradient; (2) effective permeability as a function of Air velocity; (3) Effective permeability as a function of pressure gradient**

[4] PP - polypropylene

## Open matrix Nylon mesh bonded to PP nonwoven sheathing membrane; Client C

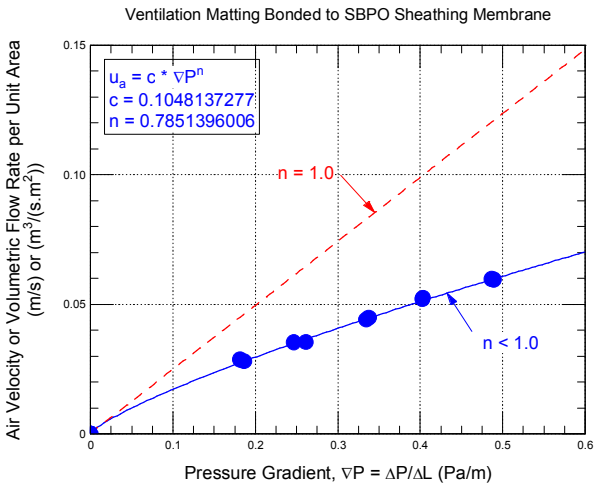


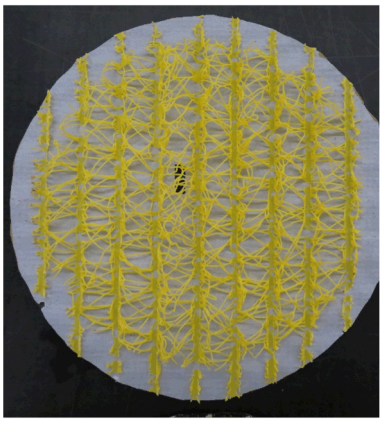

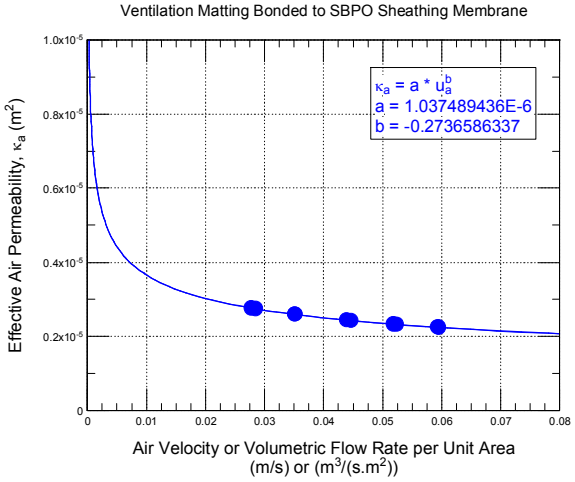


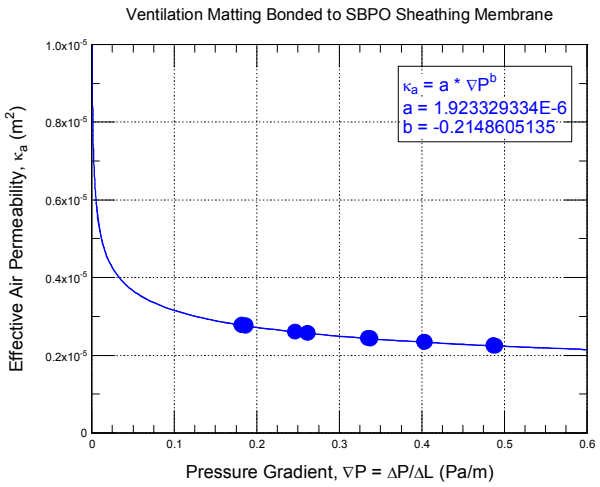


$$Q / A = u_a = c\,(\nabla P)^n \qquad \text{Eq. (7)}$$

$$\kappa_a = a\,(\nabla P)^b \qquad \text{Eq. (8)}$$

$$\kappa_a = a\,u_a^b \qquad \text{Eq. (9)}$$

| Coefficients of Eqs. (7), (8) and (9) | | |
|---|---|---|
| Eq. (7) | c | n |
| | 0.1048 | 0.7851 |
| Eq. (8) | $a = \mu_a \times c$ | b = n - 1 |
| | 1.9233E-06 | -0.2149 |
| Eq. (9) | $a = \mu_a \times c^{(1/n)}$ | b = 1 - (1/n) |
| | 1.0375E-06 | -0.2737 |

**Figure 46 – Characterization of air permeability of porous media (Open matrix Nylon mesh bonded to PP nonwoven sheathing membrane; Client C); (1) air velocity as a function of pressure gradient; (2) effective permeability as a function of Air velocity; (3) effective permeability as a function of pressure gradient**